TOPICAL REPORT

THE INITIAL ONE-DIMENSIONAL EXPANSION
OF
THE SHOCKED STATES GENERATED
BY
THE IMPACT OF CYLINDRICAL PELLETS
WITH THIN PLATES

by

Frank J. Zwarts

prepared for

NATIONAL AERONAUTICS AND SPACE ADMINISTRATION

January 15, 1965.

SPACE RESEARCH INSTITUTE
McGill University
892 Sherbrooke St. W.
Montreal 2, Canada

S U M M A R Y

14930

A theoretical investigation of the hypervelocity impact
of pellets with thin plates has been performed.

Some of the experimental work on the determination of
shocked states has been reviewed and incorporated into a purely
one-dimensional model of the impact phenomena. Based on this
model, a computer program was developed using a finite difference
technique based on the method of characteristics in order to
calculate the one-dimensional system of interacting waves. An
arbitrary equation of state could be used.

Using this program, various equations of state were
examined as to their relative merits in describing the dynamics
of the expansion process. Especially the ideal gas approximation
was critically examined and found to be applicable at high impact
velocities. Upstream flow was calculated and its dependence on
impact velocity and bumper material analyzed. For the impact
of unlike materials, the importance of the reflections from the
contact front are considered.

In addition some of the experimental techniques used in
hypervelocity impact are analyzed as to their direct application
to the verification of the foregoing theoretical predictions.

ACKNOWLEDGEMENTS

TABLE OF CONTENTS

LIST OF SYMBOLS

$\vec{V}$ - velocity vector

$\vec{\nabla}$ - divergence

U - one-dimensional particle velocity

C - velocity of sound

ρ - density

p - pressure

T - absolute temperature

E - specific internal energy

S - specific entropy

C_v - specific heat at constant volume

γ - ratio of specific heats

ω - shock velocity

K - isentropic compressibility

L - pellet length

δ - bumper thickness

r_0 - pellet radius

V - impact velocity

$\overleftarrow{S_p}$ - pellet shock

$\overrightarrow{S_B}$ - bumper shock

$\vec{C}$ - contact front

$\vec{R}_p$ - pellet rarefaction

R_B - bumper rarefaction

$\lambda_1, \lambda_2, \lambda_3$ - characteristic directions

Δp - pressure interval

γ_m, A_m, B_m - constants in Murnaghan's equation

δ_{1d} , A_{1d} - constants in the polytropic equation

$\left.\begin{array}{l} a, b, A, B \\ E_a, \alpha, \beta, \rho_0 \end{array}\right\}$ - constants occurring in Tillotson's equations

$P_c(\rho)$ - cold compression curve (zero degree isotherm)

$E_c(\rho)$ - cold compression energy

$\Gamma(\rho)$ - Gruneisen's constant

βT - electronic specific heat

Subscripts

B - bumper material

P - pellet material

C - contact front

O - initial unshocked state

I, i - characteristics

J, j - characteristics

JJ - reflected characteristics from contact front

1. GENERAL CONSIDERATIONS OF THE HYPERVELOCITY IMPACT PROBLEM

1.1 Introduction

A projectile travelling at hypervelocity $(V > 5$ km/sec) possesses large amounts of energy and momentum due to its motion. A typical value of kinetic energy would be 12 kilocal/gm. corresponding to a velocity of 10 km.sec. This may be compared to a typical explosive such as TNT which has an energy release of about 1.5 kilocal/gm.

When this projectile impacts on a target surface, this energy is explosively distributed over a very small area. Strong shock waves are formed compressing projectile and target material and generating extremely high pressures typically measured in megabars.*

The pressure of the shocked material generally is very much larger than the material strength, typically measured in kilobars.** This leads to the important simplification that the behaviour of the shocked material can be described by an inviscid, compressible fluid. This is one of the basic assumptions of many theories of hypervelocity impact and its limitations along with other approximations will be discussed in the subsequent sections.

---

* The shocks generated on impact of an aluminum projectile with an aluminum target at 10 km/sec compress material to 1.7 times its original density and raise pressure to 1.65 megabars.

** e.g., the tensile strength of aluminum at standard conditions is 1.1 kilobars.

The high thermodynamic states generated on impact cannot exist long since the surroundings are generally at much lower conditions. The pressure differential being very great (megabars $\longrightarrow$ zero for meteor impact) the resulting expansion is extremely rapid, typically time is measured in microseconds and the whole impact phenomena is essentially complete within milliseconds.*

The above discussion should give one a feel for some of the numbers involved and also indicate the difficulties that will be encountered in the analysis of the hyper-velocity impact problem, both by analytical or experimental methods.

---

* This would depend on course of the scale of the impact, the case considered here is a projectile with dimensions of the order of a cm.

1.2 The Experimental Determination of the Properties Behind Shocks in Solids

(A) Some Basic Properties of the Shock Transition

The conditions across a normal shock can be derived with great generality and are subject to relatively few restrictions. The assumptions made are:

(a) a steady state is eventually reached some distance behind the shock front

(b) the material under pressure behaves as a fluid

(c) radiation losses may be neglected

The derivation can be made in any Galilean reference system but for simplicity and clarity the following system is chosen:
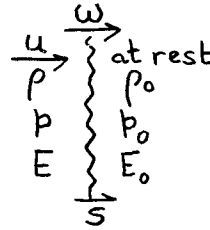
where $\vec{S}$ is a normal shock moving into a medium at rest with velocity ω . The particle velocity behind the shock with respect to the unshocked material (subscript o) is u .

Now, if conditions (a), (b) and (c) are assumed then an application of the conservation conditions across the shock gives:

Conservation of Mass

$$\rho_0 \omega = \rho \left(\omega - u \right) \tag{1.2.1}$$

Conservation of Momentum

$$p_o + \rho_o \omega^2 = p + \rho(\omega - u)^2$$

1.2.2

Conservation of Energy

$$E_o + p_o/\rho_o + \tfrac{1}{2}\omega^2 = E + p/\rho + \tfrac{1}{2}(\omega - u)^2$$

1.2.3

Combining equations 1.2.1 and 1.2.2, eliminating u, gives:

$$\omega = \sqrt{\frac{p - p_o}{\rho_o^2\left(\frac{1}{\rho_o} - \frac{1}{\rho}\right)}}$$

1.2.4

For the pressure jump from equation 1.2.2, we have

$$p - p_. = \rho_o \omega^2 - \rho(\omega - u)^2$$
$$= \rho u(\omega - u) = \rho_o \omega u$$

1.2.5

The above two equations 1.2.4 and 1.2.5 were derived using the mechanical conservation conditions only (mass and momentum). Using the energy relation equation 1.2.3, the following equation may be derived:

$$E - E_o = \tfrac{1}{2}(p + p_o)\left(\frac{1}{\rho_o} - \frac{1}{\rho}\right)$$

1.2.6

This important relation is known as the Rankine-Hugoniot condition across a shock. Its importance lies in the fact that if an equation of state of the form $E = E(\rho, p)$ is specified then equation 1.2.6 describes a unique curve in the p-ρ plane for each initial condition $(p_b, 1/\rho_0)$.

There are however, certain restrictions on the form of $E(\rho, p)$ known as the Bethe-Weyl conditions (Ref. 9) and can be stated as follows:

For stable compressive shocks to exist the equation of state has to satisfy the following inequalities:

$$\left(\frac{\partial p}{\partial s}\right)_\rho > 0$$
$$\left(\frac{\partial p}{\partial \rho}\right)_s > 0$$
$$\left(\frac{\partial^2 p}{\partial \rho^2}\right)_s > 0$$

$$1.2.7$$

These are satisfied for nearly all materials* that we are concerned with and thus need not be dwelled upon.

---

* An important exception to this is phase changes where discontinuities in Hugoniot curves occur violating conditions 1.2.7

For equations of state satisfying the above conditions, the Hugoniot curve takes on the following general shape.

Hugoniot Curve
for a typical
material
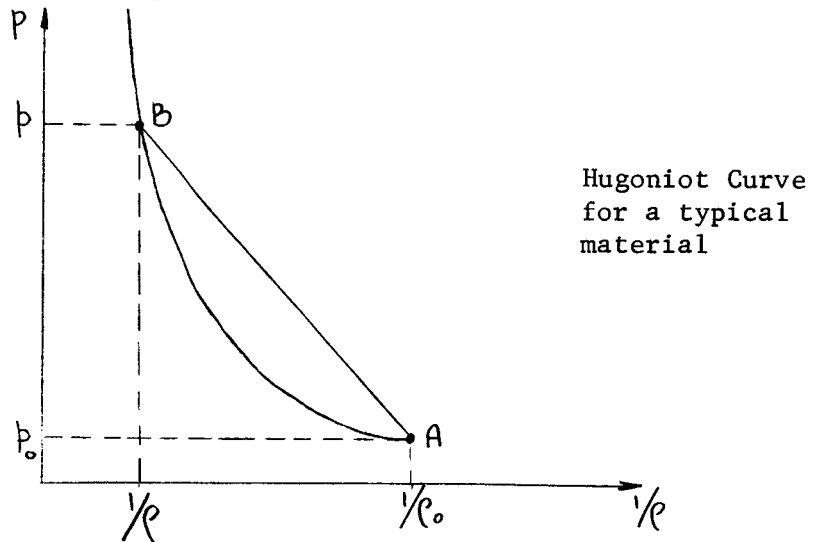
Where point A (p_o, $1/\rho_o$) is the initial state and B (p, $1/\rho$) is the condition behind the shock. One important fact is that the slope of line A-B is directly related to the speed of the shock through equation 1.2.4

i.e. $\omega = \sqrt{\dfrac{p - p_o}{\rho_o^2 \left(\frac{1}{\rho_o} - \frac{1}{\rho}\right)}} = \sqrt{\dfrac{-(SLOPE)}{\rho_o^2}}$

(B) Experimental Determination of the Hugoniot Curve

Of the relations derived in the previous section, two assume special importance in the experimental determination of shock Hugoniots. They are equations 1.2.1 and 1.2.5 which may be re-written as:

$$\rho = \rho_o \frac{\omega}{\omega - u} \qquad\qquad 1.2.8$$

and $p = p_o + \rho_o\, u\, \omega$

$$1.2.9$$

Assuming the initial states to be known, the density ρ and the pressure p , can be determined from an experimental observation of the shock velocity, ω , and the particle velocity behind that shock, u . In this way a point is located on the Hugoniot curve which passes through the initial conditions (p_o , ρ_o).

In general velocity measurements can be made quite accurately and a number of experimental techniques have been developed in the last 15 years (see Refs. 1, 2, 3, 4, 5 & 6).

In order to satisfy assumption (a) and (b) of the section (A), sufficiently strong shocks have to be generated so that (a) the shock thickness does not approach the physical dimensions of the experiment, and (b) the shocked pressure is sufficiently above the yield strength of the material so that the material behaves as a fluid.

To produce shocks of this strength requires the practically instantaneous generation of very high pressures (at least 10 - 100 kilobars) which have to be held constant over a period of time (approx. 1 μ sec) in order for shock to be of constant strength.

Two basically different techniques have been developed in order to fulfill the above requirements.

The Direct Contact Method

In this method an explosive lens (producing a plane detonation wave) is placed in direct contact with the sample. The interaction of the detonation with the surface of the sample produces the necessary pressure for a short period of time. The pressure produced is generally not perfectly constant, as is required, but the shock attenuation due to this is generally small (see Ref. 4).

The measurements made are the shock velocity and the free-surface velocity of the target material as the shock emerges from the end of the sample. It has been shown (Refs. 1 and 4) that this velocity is nearly twice the particle velocity behind the shock for most materials with very little deviation (at least for shocks generated within the experimental regime of this method.)

Shock pressures are limited in this method to the range 50 - 500 kilobars. The lower limit arises due to failure of explosive to detonate. For pressure below and above this region a substantially different technique is used.

The Flying Plate Method

In this method a plate is explosively accelerated and impacts on a target. Various methods of acceleration are used but for shock Hugoniot studies an explosive-lens system is generally used to obtain maximum impact velocities (up to 14 km/sec, Ref.6) using relatively short runs (several cms).

The particle velocity, in this case, can be directly deduced from the velocity of the free-running plate. If projectile and target are of the same material then the particle velocity is exactly half the impact velocity (see section 2.4) For the impact of different materials the particle velocities can be obtained through the impedance matching of bumper with projectile material provided the Hugoniot curve of one of these is known.

Using this method pressures as high as 9 megabars have been reported (Ref. 6). The limiting factor in this method seems to be the energy release possible in a single explosive stage and possibly multiple staging or even a low yield nuclear device have been suggested (Ref. 8) to bring pressures up to the ultimate using this technique (several hundred megabars). The limit being the maximum acceleration a plate will take without breaking up or being heated to its melting point by the explosive substance.

(C) <u>Isentropic Compressibility Behind a Shock</u>

At some time following the initial formation of the impact shocks, the shocked material will be expanded. It is therefore necessary to determine the compressibility of the material in the shocked state.

This is done by determining the speed of sound in the shocked medium through shock attenuation experiments (Ref. 7), the speed of sound being related to the isentropic compressibility by:

$$K = \rho_o \left(\frac{\partial p}{\partial \rho} \right)_s = \rho_o C^2 \qquad\qquad 1.2.10$$

The actual experimental technique is much the same as in the flying plate method except that the projectile release wave* is allowed to overtake and attenuate the target shock, by using a relatively thick bumper.

Knowledge of the shock decay curve enables one to pin-point where the projectile rarefaction first over-takes the bumper shock. If the shock Hugoniot for the material is known from previous experiments, the speed of sound in the shocked material can then be determined.

---

* formed when projectile shock reaches free surface

The values for the isentropic compressibility determined in this manner agree very closely with those calculated from the various equations of state (see section 1.3 and Refs. 7 and 11), thus providing an important check on their validity.

1.3   The Equation of State

In dealing with condensed media such as shocked solid materials, the usual approximate relations developed for gases do not apply and new equations based on solid state theories have to be developed.

A difficulty arises here due to the fact that we are generally interested in the complete expansion from megabars to a vacuum. For highly shocked materials the expansion into vacuum is very much like a gas (i.e. density $\longrightarrow$ zero as pressure $\longrightarrow$ zero). For not so strongly shocked materials the density does not go to zero as the pressure decreases to zero, since the shocks do not have sufficient energy to vapourize the material. Unfortunately the latter case is true for most of the experimental range available and only at impact velocities approaching 15 km/sec. do most metals start to behave like gases in the expansion phase of the impact phenomena.

Many non-metals, however, do vapourize before this (e.g. camphor) but they are not as well known thermodynamically as metals and a great deal of uncertainty exists about even the heat of vapourization (especially plastics).

(A) Condensed States

In the high density shocked phase of the expansion $\left(\left| \rho / \rho_0 \right. \right\rangle 1 \right)$ most materials behave similarly regardless of the impact velocity and the equations developed in solid state physics for ultra-high pressures are expected to apply. One of the best known of these is the Mie-Gruneisen equation of state. It has been used with reasonable success by Walsh et al. (Refs. 1, 2, 3 and 4) in the early Los Alamos work on shocked solid states and in a slightly modified form by Al'tshuler et al. (Refs. 5, 6) in the corresponding Russian work.

The assumptions upon which the Mie-Gruneisen equation is based are:-

(a)   Only hydrostatic pressure is considered (i.e. fluid model).

(b)   Sufficiently high temperatures for C_v and the Gruneisen constant, Γ , to become essentially temperature-independent.

(c)   The lattice dynamics can be represented by harmonic oscillators. As the solid nears its melting point, this is not strictly true and vibrations become anharmonic.

(d)   Effects of free electrons are neglected. This assumption is valid up to temperatures of about $5000^\circ K$ when electronic additions to the specific heat, pressure and energy become significant.

Under these conditions, the Mie-Gruneisen equation may be written in the following form:

$$p - p_c(\rho) = \rho \, \Gamma(\rho) \left(E - E_c(\rho) \right)$$

1.3.1

where $p_c\ (\rho)$ and $E_c\ (\rho)$ are the pressure and
internal energy at 0^oK respectively. $\Gamma(\rho)$ is the
so called Gruneisen constant, a weak function of
density.

At sufficiently high temperatures* we may write
for $E \simeq E_c + C_v T$

$$1.3.2$$

and equation 1.3.1 becomes

$$p - p_c(\rho) = \rho \, \Gamma(\rho) C_v T \qquad 1.3.3$$

The dependence of the Gruneisen constant on density
may be deduced from the following formula due to
Slater (Ref.10):

$$\Gamma(\rho) = -\frac{2}{3} + \frac{1}{2} \left\{ \frac{\left(\partial^2(1/\rho)/\partial p^2\right)}{\rho\left(\partial(1/\rho)/\partial p\right)} \right\} \qquad 1.3.4$$

This formula although based on some rather crude
assumptions does give quite surprisingly good
results at low pressures and since dependence of
Γ on ρ is only slight its use seems to be
justified.

---

* above Debye temperature, which usually is just slightly
above room temperature.

The function p_c (ρ) can then either be
determined from static data or deduced through
equations 1.3.2, 1.3.3 and 1.3.4 from the shock
Hugoniot data. Although these two methods do cover
different ranges of pressure and density, Walsh et al.
(Ref. 4) finds that they join smoothly and the use
of the Gruneisen equation of state is justified at
least for a region in the neighbourhood of the shock
Hugoniot.

Al'tshuler (Ref. 6) modified equation 2 to allow
for the pressure of free elections in the metallic
state. The modified equation has the form:

$$E = E_c(\rho) + C_v T + \frac{1}{2} \theta(\rho) T^2 \qquad \text{1.3.5}$$

where γ is the electronic specific heat and θ a
function of density only

$$\theta(\rho) = \theta_0 \left(\rho / \rho_0\right)^2 \qquad \text{1.3.6}$$

This modification is expected to give more accurate
results in the high pressure regions and good agreement
is noted by extrapolating their results unto results
obtained using the Thomas-Fermi model of the atom which
only starts applying at pressures over 50 megabars
(the highest experimental pressure being 9 megabars).

Most of these equations and others like it
(see Ref.11) although being the most accurate
presently available for the calculation of condensed
states are cumbersome to apply, requiring a great
amount of numerical work. Tillotson (Ref. 12) has
developed a semi-empirical equation which is
relatively simple and convenient to use in numerical
work.

$$p = \left\{ a + \frac{b}{\frac{E}{E_0 \eta^2} + 1} \right\} E\rho + A\mu + B\mu^2$$

1.3.7

where $\eta = \rho/\rho_0$ and $\mu = \eta - 1$.

This equation represents a best-fit extrapolation
between Thomas-Fermi data at ultra high pressures and
shock wave data at lower pressures. The estimated
accuracy (from comparison with Walsh's and Al'tshuler's
data) is $\pm$ 5% for shock Hugoniot pressures and $\pm$ 8% for
isentropic expansion pressures.

(B) Expanded States

There still remains the problem of the expansion
of the shocked material at low densities (i.e. $\rho/\rho_0 < 1$).
If material has sufficient energy $(E > E_s)$ at these
lower densities it will behave as a gas and an equation
different from those developed for condensed states
has to be used.

Where E_s is a limiting energy at which gas will start to condense and is related to the vaporization energy.

Tillotson (Ref. 12) here again developed a semi-empirical equation of the following form:

$$p = aE\rho + \left\{ \frac{bE\rho}{\frac{E}{E_0 \eta^2}+1} + A\mu e^{-\beta\left(\frac{\rho_0}{\rho}-1\right)} \right\} e^{-\alpha\left(\frac{\rho_0}{\rho}-1\right)^2} \qquad 1.3.8$$

The constants in equations 1.3.7 and 1.3.8 are listed in TABLE III for some typical materials. For very low densities $\left(\frac{\rho_0}{\rho} - 1\right)^2 >>> 1$ and the equation reduces to the ideal gas equation

$$p = aE\rho \qquad 1.3.9$$

If the internal energy, E, is less than a certain minimum E_s required for vaporization then the material is assumed to partially condense and the condensed form equation 1.3.7 is used.

The above although not exact gives the approximate behaviour of the expansion states with an estimated accuracy within $\pm$ 7%.

1.4 General Equations of Motion

As mentioned in section 1.1, the hydrostatic

pressure behind the shocks produced in hypervelocity

impact is at least several orders of magnitude above

any rigidity effect of the material. The shocked

material can thus be treated as a fluid. The validity

of this assumption has been tested by comparing the

pressure obtained from dynamic measurements (as in

section 1.2)with the static pressure measurements made

by Bridgeman up to 100 kilobars. For aluminum, the

agreement is found to be entirely satisfactory down to

about 20 kilobars (Ref. 20).

In addition, we neglect any effects due to

viscosity and heat conduction. This assumption depends

on the physical size of the phenomena. These effects

are usually confined to small regions where the

gradients in velocity and temperature are very large.

These regions can then be represented either by shock

or shear discontinuities to account for their

presence. It has been estimated that these effects are

confined to regions of the order of 10^{-3} cm under most

conditions (Ref. 4).

The next assumption is that of thermodynamic

equilibrium. Again, if these regions of large gradients

are avoided the fluid can be assumed in equilibrium so

that any two independent thermodynamic parameters are

sufficient to determine the state of the fluid at any point.

Making the usual assumptions of continuity, homogeneity, and isotropy we can use a continuum model and write the conservation equations in a differential form for a compressible, inviscid, non-heat-conducting fluid.

Continuity Equation

$$\frac{D\rho}{Dt} + \rho \, \vec{\nabla} \cdot \vec{V} = 0$$

1.4.1

Equation of Motion

$$\rho \frac{D\vec{V}}{Dt} + \vec{\nabla} p = 0$$

1.4.2

Energy Equation

$$\frac{DE}{Dt} + p \frac{D\left(\frac{1}{\rho}\right)}{Dt} = 0$$

1.4.3

where $\dfrac{D}{Dt} = \dfrac{\partial}{\partial t} + \vec{V} \cdot \vec{\nabla}$

Equation of State

$$p = p(E, \rho)$$

1.4.4

We have in addition neglected radiative heat transfer which might be a questionable assumption for ultra-high velocity impacts (greater than 75 km/sec) but seems reasonable in the normal velocity range (Ref. 21).

One important property of the system of equations (1.4.1 - 1.4.4) is that they can be scaled in length and time (i.e. if length-scale is changed by a factor K then time-scale is also changed by a factor K). This enables us to calculate the flow field for one particular size and then scale results to any size of that particular geometry.

2. THE IMPACT OF PELLETS WITH THIN PLATES

2.1 Introduction

In 1946, Whipple (Ref. 19) suggested that the kinetic energy of a meteor could be used to destroy it on impact with a thin bumper, or shield, spaced a distance away from the main skin of a space vehicle. In this way the highly shocked meteor and bumper material can expand laterally subsequent to the original impact, distributing the previously concentrated projectile energy over a large volume. Provided the vehicle skin is far enough away from the shield, the energy and momentum reaching it per unit area will not be sufficient to cause serious damage.

That the general behaviour of such a scheme is correct has been shown qualitatively by a photographic study in a previous report in this series (Ref. 15). A short sequence of frames from one of these shots is reproduced here in Fig. 1 and serves to illustrate the main features of the flow subsequent to the impact of a cylinder with a thin plate.

At present however, the upper limit of the experimentally obtained velocities ($\sim$ 11 km/sec) is only the lower limit of expected meteor velocities (10 - 75 km/sec.) Therefore, in order to extrapolate the experimental results to these higher velocities a sound theoretical foundation is needed.

Previous analytical approaches in this series
(Refs. 13 and 14) have used an ideal gas equation
of state with a specific heat ratio (polytropic
exponent) of approximately three. This choice was
due first of all to the inherent simplicity of the
ideal gas approach and also due to the reasonably good
agreement obtained with experimentally determined shock
data. It is one of the purposes of this report to
critically examine some of the previous assumptions
made, especially the ideal gas assumption, and to
suggest possible improvements which would still enable
them to be used but with greater accuracy.

At the same time the basic one-dimensional model
of Ref. 13 is slightly reformulated to account for the
equation of state effects. This model is then used to
calculate the flow field subsequent to impact, in
particular the interaction of the rarefaction waves
formed when the impact shocks reach the end of both
the pellet and the bumper. It is hoped that a one-
dimensional consideration of this type will account
for much of the upstream flow observed in the
photographic study of Ref. 15.

FIGURE 1 - FRAMING CAMERA SEQUENCE

Impact of a 12.7 mm. diameter, 8.9 mm. long Lexan plastic cylinder against a 2.54 mm. thick Nylon bumper plate. The impact velocity was 6.0 Km/sec. The time between exposures 1.07 μ sec. and the exposure time 0.45 μ sec. The range pressure was 0.2 microns of mercury.
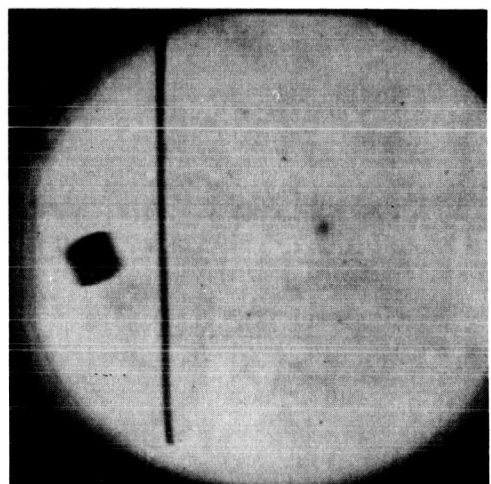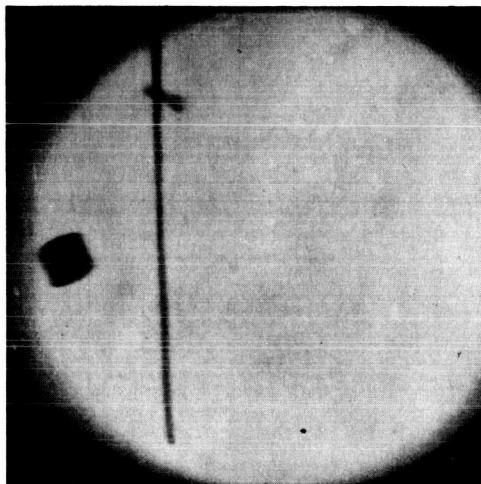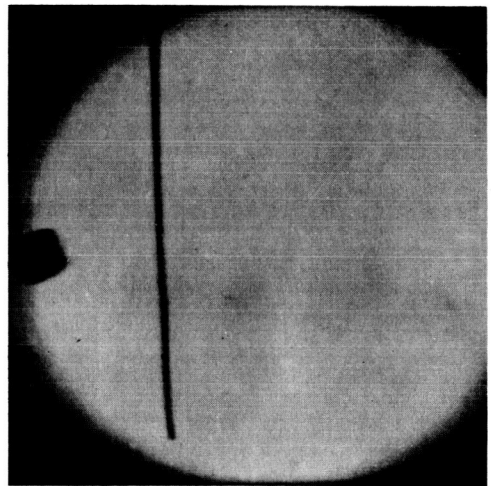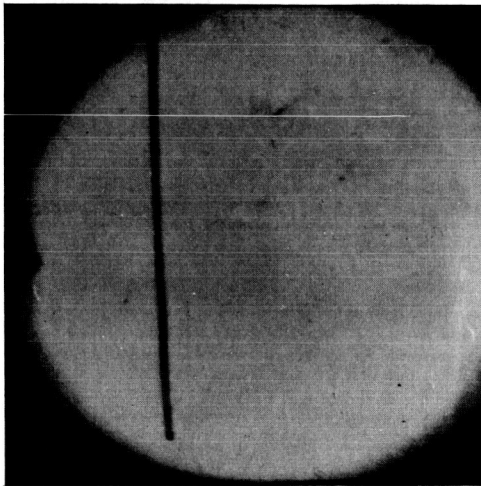
FIG. 1 (CONT'D)
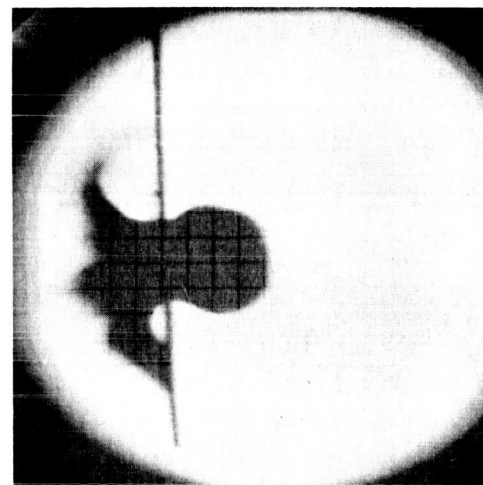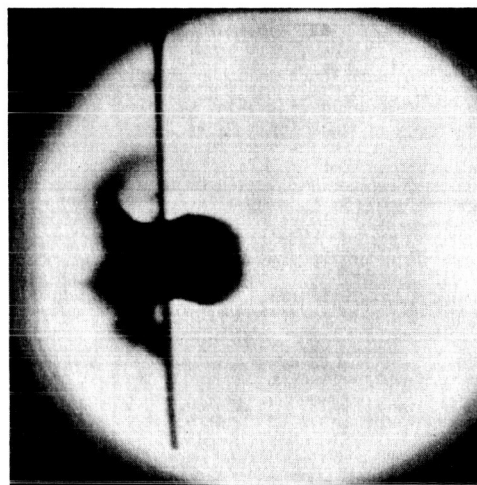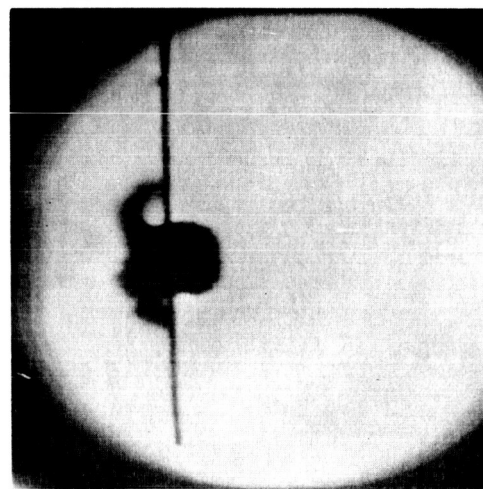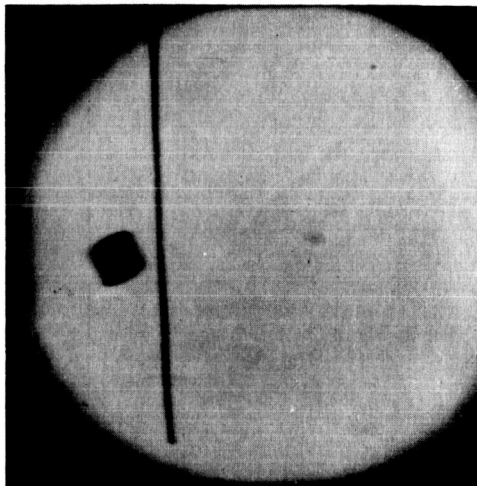
2.2 Geometry of the One-Dimensional Formulation

In order to reduce the problem down to its simplest form, we consider the axi-symmetric impact of a right-cylindrical pellet of length L, and radius r_0, with a thin bumper plate of thickness δ . The velocity V, of the pellet is directed along its axis of symmetry and is at right angles to the bumper.

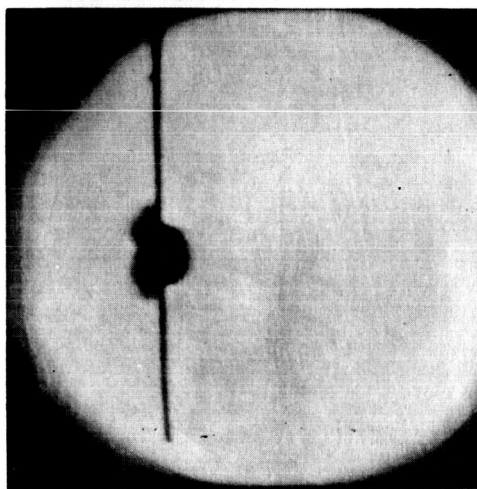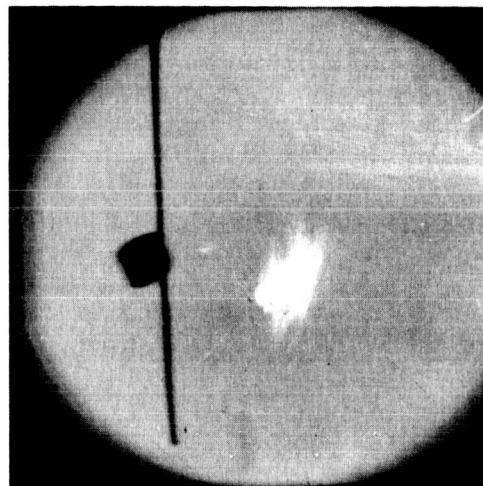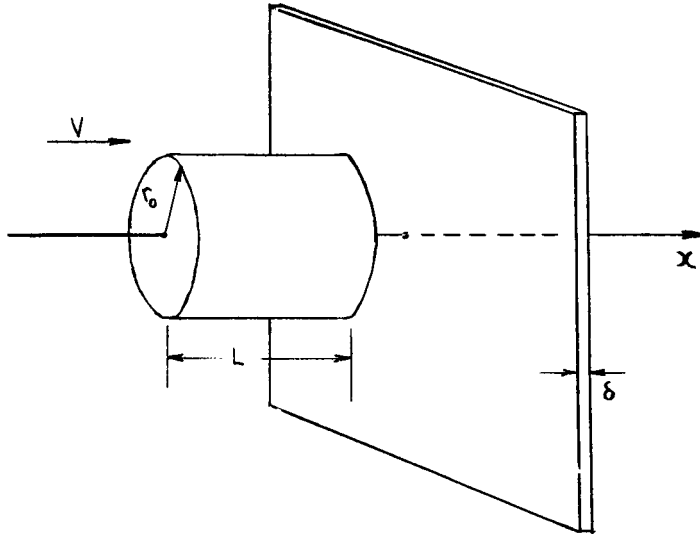Furthermore, we make the gross simplification that the cylindrical edge effects can be neglected. This will only be strictly true for disk-like pellets with very small length to diameter ratios (i.e. $L/2r_0 \ll 1$). A one-dimensional analysis however, will still be valid for longer pellets at the axis of symmetry as long as the radial interactions have not had time to reach the center.

2.3 Shock System

Using the above idealization, we have that on the moment of impact plane shock waves are developed, one entering the pellet, $\overleftarrow{S}_p$, and the other, S_B, entering the bumper material. The shock-wave system thus generated is illustrated in the following sketch.
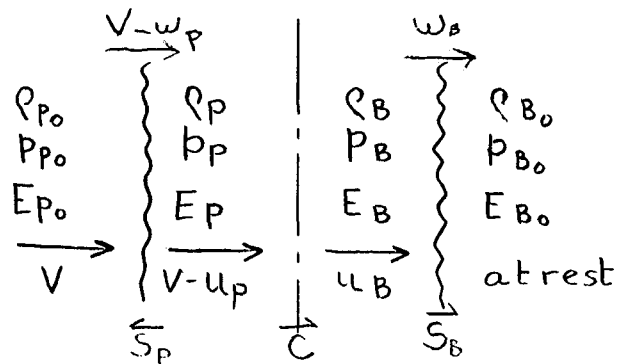
We have shown previously that for a normal shock the following relations hold with great generality

$$\frac{\rho}{\rho_0} = \frac{\omega}{\omega - u} \qquad\qquad 2.3.1$$

$$p = p_0 + \rho_0 u \omega \qquad\qquad 2.3.2$$

$$E - E_0 = \frac{1}{2}\left(p + p_0\right)\left(\frac{1}{\rho_0} - \frac{1}{\rho}\right) \qquad\qquad 2.3.3$$

These equations apply to both the pellet and bumper shocks giving six equations in the 10 unknown p_p, p_B, ρ_p, ρ_B, E_p, E_B, u_p, u_B, w_p, and w_B.

The remaining four equations are obtained from the equations of state in the form

$$E = E\left(\rho, p\right)$$ 2.3.4

and from the continuity of velocity and pressure across the contact front, $\vec{C}$, between the pellet and bumper material

$$V - u_p = u_B$$ 2.3.5

$$p_p = p_B$$

2.3.6

Experimental determination of shocked states such as described in section 1.2 give a single relation in p and ρ which essentially is a combination of equations 2.3.3 and 2.3.4 called the Hugoniot curve. TABLE I gives a curve fit for Hugoniot curves for various materials.

Using these experimental curve fits the system of equations 2.3.1 - 2.3.6 was solved by an iterative technique for various material combinations.

2.4 Interaction Times and Distances

When the shock waves $\overleftarrow{S}_{\text{\i}}$ and $\overrightarrow{S}_B$ reach the free surfaces of the pellet and bumper respectively centered rarefaction waves $\overrightarrow{R}_{\text{\i}}$ and $\overleftarrow{R}_B$ are set up in order to satisfy the zero pressure boundary condition at these surfaces. The wave system subsequent to this interaction is best illustrated by a x-t diagram as follows.
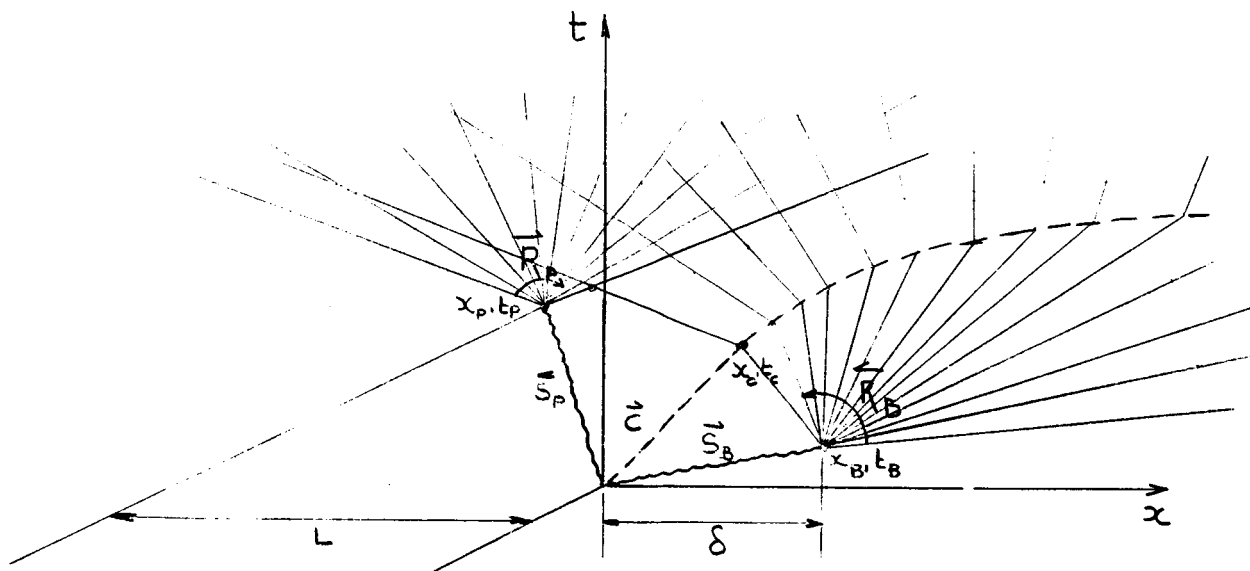
The points of initiation of the rarefaction waves are the points where the shocks reach the free surfaces. These are found as follows:

Bumper:
$$\left.\begin{array}{l} t_B = \delta/\omega_B \\[6pt] x_B = \delta \end{array}\right\} \qquad 2.4.1$$

Pellet:
$$\left.\begin{array}{l} t_p = L/\omega_P \\[6pt] x_p = L\left(\frac{v}{\omega_P} - 1\right) \end{array}\right\} \qquad 2.4.2$$

The head of a rarefaction wave moves into a medium
at the velocity of sound of that medium. In general for
any characteristic (of which the head and tail of a
rarefaction are just special cases) the slope is given by:

$$\frac{dx}{dt} = u + c \qquad \text{for a } \lambda_1 \text{ characteristic}$$

$$\frac{dx}{dt} = u - c \qquad \text{for a } \lambda_2 \text{ characteristic}$$

Now if u_B, C_B and C_P are known from the previous
section we can find the points where rarefactions start
to interact with contact front and each other.

Contact front: -

$$\left.\begin{aligned} t_c &= \frac{x_B}{C_B} + t_B\left(1 - \frac{u_B}{C_B}\right) \\ x_c &= u_B t_c \end{aligned}\right\} \qquad 2.4.3$$

Interaction: -

$$\left.\begin{aligned} t_I &= \frac{\left(x_c - x_P\right) + t_P\left(u_B + C_P\right) - t_c\left(u_B - C_P\right)}{2a_P} \\ x_I &= x_P + \left(u_B + c_P\right)\left(t_I - t_P\right) \end{aligned}\right\} \qquad 2.4.4$$

Excluded from the above is the case where the
rarefactions reach the shocks before shocks reach free
surfaces. The resulting shock attenuation results in
non-isentropic flow which requires slightly different
treatment. This limits bumper to pellet length ratios
(δ/L) to greater than 1/5 for most material combinations.

The interaction points are plotted as a function of the bumper thickness and impact velocity for various material combinations in Figs. 2, 3 and 4. The thermo-dynamic data for the shocked states was again obtained from Al'tshuler's experiments (Refs. 6 and 7).
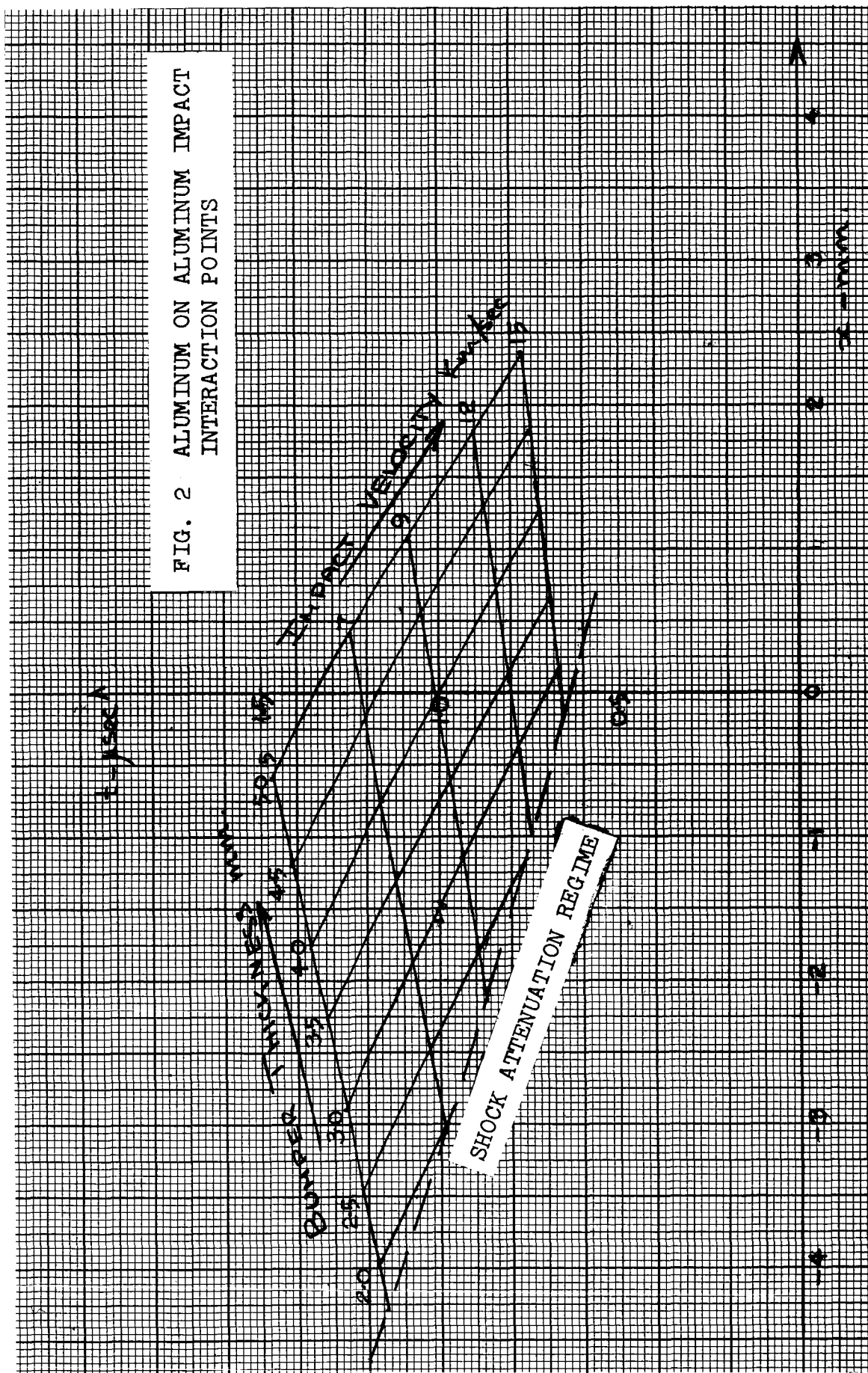
FIG. 2 ALUMINUM ON ALUMINUM IMPACT
INTERACTION POINTS

FIG. 3 ALUMINUM ON COPPER IMPACT
INTERACTION POINTS
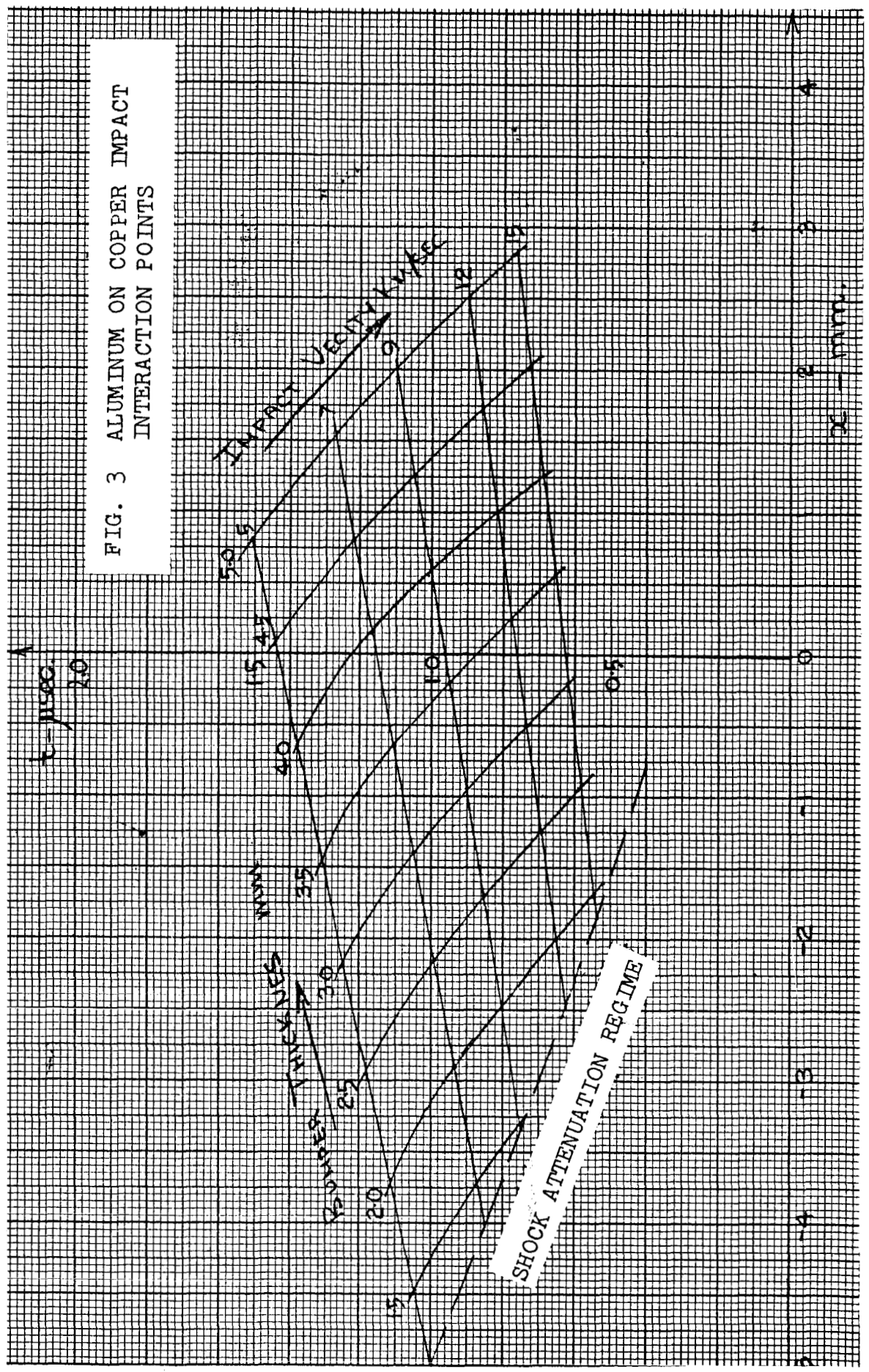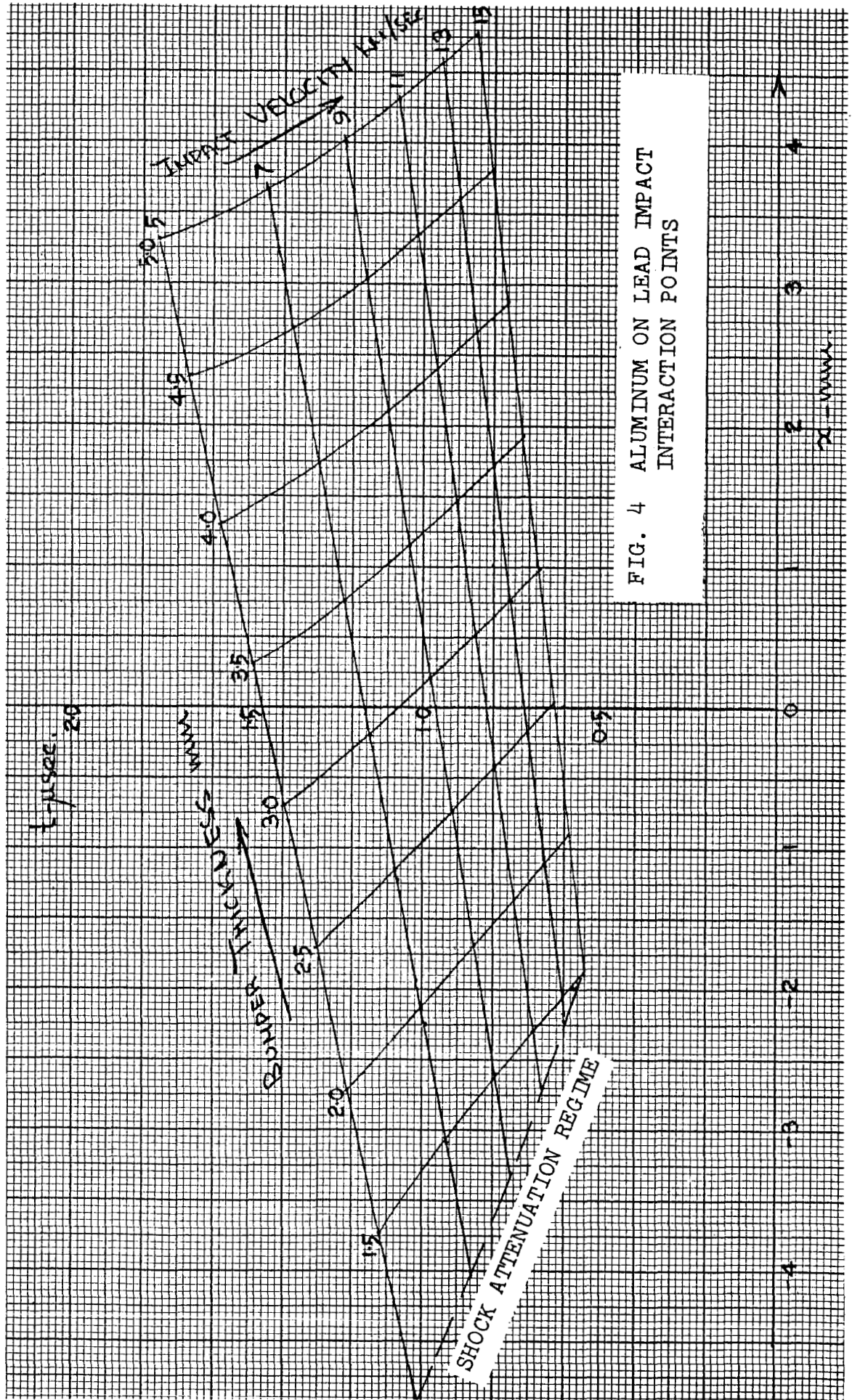
FIG. 4 ALUMINUM ON LEAD IMPACT
INTERACTION POINTS

2.5 The Interaction Region

At times greater than t_I the flow no longer consists
of simple waves of one family of characteristics and the
interaction of the rarefactions has to be considered.
Explicit solutions of this problem exist (Ref. 17) but
these are complicated and applicable only to ideal gases
and then only for certain specific values of the ratio
of specific heats, γ.

In order to determine the effect of more realistic
equations than the ideal gas approximation resort has to
be made to numerical techniques. The method used here is
a finite difference technique based on the method of
characteristics developed in Appendix A.

In order to apply the method, we need two points A
and B where all the flow parameters are known. We can
then determine the corresponding parameters at a point P,
which is the intersection of the λ characteristic
through A and the λ characteristic through B as
illustrated in the following figure.
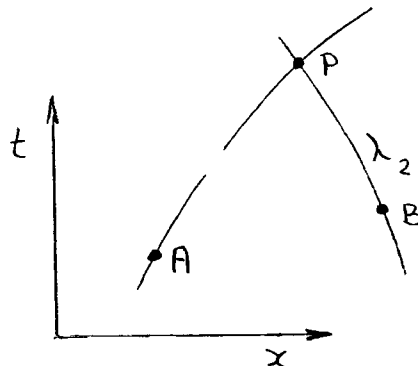
Making the basic assumption that the points are chosen sufficiently close together so that the dependent variables can be taken to vary linearly between adjacent points, we write the characteristic equations (A.8 and A.9) in the following finite difference form.

$$\left.\begin{array}{l} x_P - x_A = (u+c)\lambda_1 (t_P - t_A) \\ x_P - x_B = (u-c)\lambda_2 (t_P - t_B) \end{array}\right\} \qquad 2.5.1$$

and

$$\left.\begin{array}{l} u_P - u_A = -\frac{1}{(\rho c)\lambda_1}(p_P - p_A) \\ u_P - u_B = \frac{1}{(\rho c)\lambda_2}(p_P - p_B) \end{array}\right\} \qquad 2.5.2$$

As a first approximation, the values of the quantities subscripted λ_1 and λ_2 may be taken as those values at the points A and B respectively. This corresponds to a linear extrapolation and enables one to solve equations 2.5.1 and 2.5.2 explicitly for point P in terms of quantities at points A and B only, knowing of course, the equation of the isentrope linking ρ , p, and c.

The second approximation then takes the average values for λ_1 and λ_2 between points A and P and points B and P respectively. The values for P being determined previously from the linear extrapolation.

This procedure is in essence a trapezoidal rule type
of numerical integration of the variables along the
characteristics.

The above enables us to solve a characteristic
mesh provided we always have two points to start the
process.

In order to illustrate the method, we take the
following characteristic net.
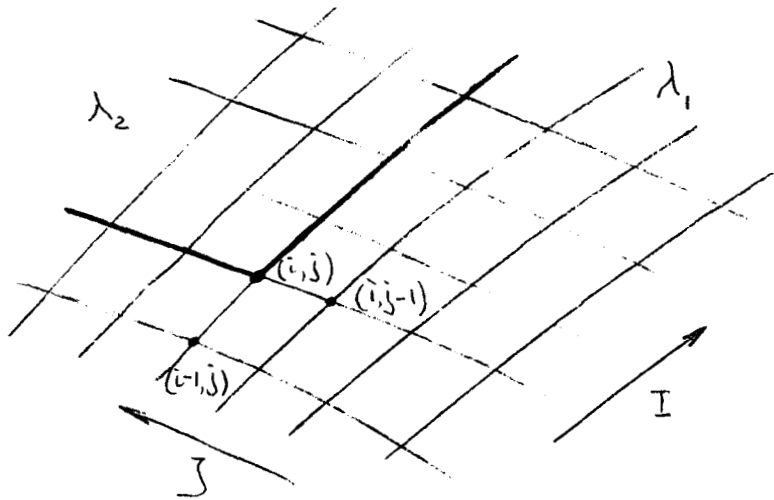
The λ_2 characteristics are numbered I and the λ
characteristics J. The point I = i, J = j is an
undetermined point within the net. Now if we assume
that all points I $\angle$ i, J and I, J $\angle$ j have been
previously determined, we can apply equations 2.5.1
and 2.5.2 to find the undetermined points.

Modifying equations 2.5.1 and 2.5.2 to include the subscripted notation of the characteristic net and solving them for the variables u (i, j), x (i, j), t (i, j), we have:

$$u(i,j) = \frac{\left\{(\rho c)_R \, u(i-1,j) + p(i-1,j)\right\} + \left\{(\rho c)_L \, u(i,j-1) - p(i,j-1)\right\}}{\left((\rho c)_R + (\rho c)_L\right)}$$

$$2.5.3$$

where

$$\left.\begin{array}{l} (\rho c)_R = \rho(i-1,j) \cdot c(i-1,j) \\ (\rho c)_L = \rho(i,j-1) \cdot c(i,j-1) \end{array}\right\}$$

$$2.5.4$$

for the first approximation. In the second approximation the mean values are indicated by:

$$\left.\begin{array}{l} (\rho c)_R = \rho\left(i-\tfrac{1}{2},j\right) \cdot c\left(i-\tfrac{1}{2},j\right) \\ (\rho c)_L = \rho\left(i,j-\tfrac{1}{2}\right) \cdot c\left(i,j-\tfrac{1}{2}\right) \end{array}\right\}$$

$$2.5.5$$

furthermore

$$p(i,j) = p(i-1,j) - (\rho c)_R \left[u(i,j) - u(i-1,j)\right]$$

$$2.5.6$$

From this we can determine ρ (i, j) and c(i, j) through the equation of the isentrope.

The location of the next mesh point is then given by:

$$t\left(i,j\right) = \frac{\left\{CR.t\left(1-1,j\right)-x\left(i-1,j\right)\right\} - \left\{t\left(i,j-1\right)-x\left(i,j-1\right)\right\}}{\left(CR-CL\right)} \qquad 2.5.7$$

where

$$\left. \begin{array}{l} CR = u\left(i-\tfrac{1}{2},j\right) + c\left(i-\tfrac{1}{2},j\right) \\ CL = u\left(i,j-\tfrac{1}{2}\right) - c\left(i,j-\tfrac{1}{2}\right) \end{array} \right\} \qquad 2.5.8$$

for the second approximation.

Furthermore

$$x\left(i,j\right) = x\left(i-1,j\right) + CR\left(t\left(i,j\right)-\left(i-1,j\right)\right) \qquad 2.5.9$$

This then demonstrated how points within the interaction region may be calculated. It remains to be shown how the process may be started at the boundaries of the interaction region.

2.6 Boundaries of the Interaction Region

In order to start the procedure described in the previous section, we need conditions along the characteristic lines J = 1 and I = 1. These are the first characteristics crossing the rarefaction waves $\overleftarrow{R}_B$ and $\overrightarrow{R}_C$ respectively.

For the bumper rarefaction, $\overleftarrow{R}_B$, we have the following geometry:
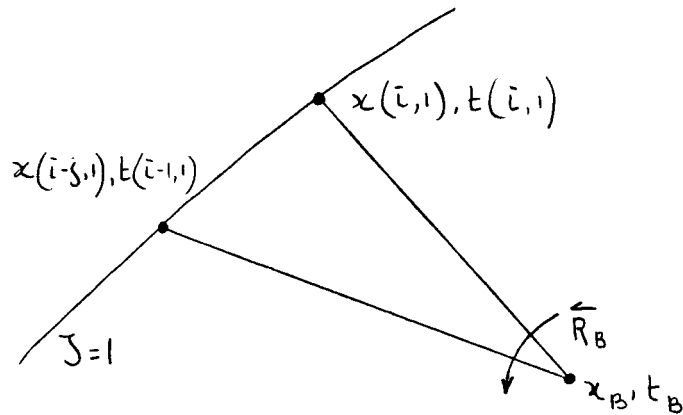
where for the moment we have assumed that the centered rarefaction $\overleftarrow{R}_B$ does not pass through a contact front. The interaction of the wave with a contact front will be discussed in the next section and the present analysis is only strictly applicable to the impact of like materials.

At this point it becomes necessary to specify our interval or grid size. Since the free surface boundary condition is one of pressure (p = o at the free surface), we define our interval Δ p so that

$$p(i,1) = p(i-1,1) + \Delta p$$

2.6.1

From equation 2.6.1 we can determine ϱ (i, 1) and c (i, 1) through the specified isentrope.

The velocity, u (i, 1) can then be determined from the first of equations (A.9) as follows:

$$u(i,1) = u(i-1,1) - \Delta p \Big/ \Big(\varrho(i-\tfrac{1}{2},1) \cdot c(i-\tfrac{1}{2},1) \Big)$$

2.6.2

Where the subscript (i $-\tfrac{1}{2}$) as before indicates the average value of the parameters between (i -1) and (i).

The location of point (i, 1) can then be found from equations 2.5.7 and 2.5.9 as

$$t(i,1) = \frac{\{CR \cdot t(i-1,1) - x(i-1,1)\} - \{CL \cdot t_B - x_B\}}{(CR - CL)}$$

2.6.3

and $$x(i,1) = x(i-1,1) + CR\Big[t(i,1) - t(i-1,1) \Big]$$

2.6.4

where
$$CR = u(i-\tfrac{1}{2},1) + c(i-\tfrac{1}{2},1) \Big\}$$
$$CL = u(i,1) - c(i,1) \qquad \Big\}$$

2.6.5

The second approximation is used here throughout since an explicit form can be obtained and no iteration is necessary.

For the pellet rarefaction, $\vec{R}_p$, exactly the same procedure is used except the subscripts I and J are interchanged. The initial condition x (1, 1), t (1, 1) is the same for both rarefaction waves and is previously calculated as x_I, t_I.

In the above, we have neglected the interaction of the bumper rarefaction with the contact front (for dissimilar materials) and we go on to the next section to discuss the necessary modifications.

2.7 Interaction with a Contact Surface

Since the bumper is always considerably thinner than the pellet, the bumper rarefaction always inter- acts first with the contact front before meeting the pellet rarefaction. We therefore, consider the problem of a centered rarefaction $\overleftarrow{R_B}$ interacting with a contact front $\overrightarrow{C}$. The geometry of the problem is as follows:
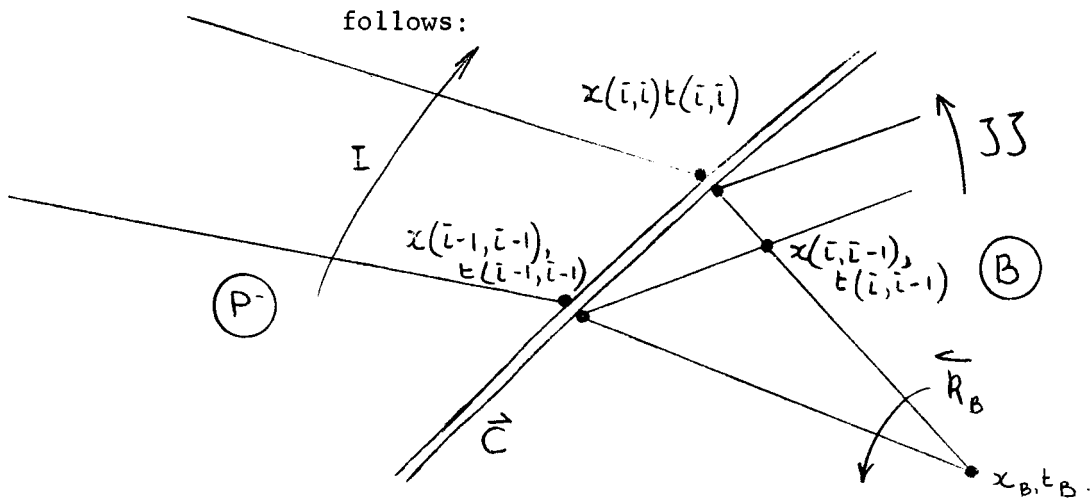
In order to differentiate between materials, we subscript pellet material, P and bumper material B.

The basic conditions across a contact front are:

$$U_P = U_B \qquad\qquad 2.7.1$$

$$P_P = P_B$$

and $\qquad\qquad 2.7.2$

The first condition governs the motion of the front and the second enables one to transfer thermodynamic quantities across the front.

From previous calculations we know conditions at points x_C, t_C and x_B, t_B. There will be both reflected and transmitted waves from the contact front. Note that the transmitted waves are simple since they are entering a region of constant properties (see Appendix B).

The first reflected characteristic $JJ = 1$ is found in exactly the same manner as in the previous section, the only difference being the replacement of x_C, t_C for x_I, t_I.

To start the calculation of the next row JJ, we need to calculate the next point along the contact front. For points on the contact front $I = JJ$. Taking any point (i, i) on the contact front, we assume that all points previous to it have been determined for all I.

The fact that the transmitted characteristics are of only one family (simple waves) enables us to use the following equation

$$u\left(\bar{\iota}\right) - u\left(\bar{\iota}-1\right) = -\frac{1}{(\rho c)_R}\left(p(\bar{\iota}) - p(\bar{\iota}-1)\right)$$

for the variation from one characteristic to another, properties being constant along any one characteristic. In addition, we have the conditions along the left running characteristic intersecting at (i, i) plus the constant pressure condition across the contact front itself.

43

In terms of these conditions, we can then solve

for u (i, i) and p (i, i) as follows:

$$u(i,i) = \frac{(\rho_P C_P)_R \cdot u(i-1,i-1) + p(i-1,i-1) + (\rho_B C_B) \cdot u(i,i-1) - p(i,i-1)}{(\rho_P C_P)_R + (\rho_B C_B)_L}$$

2.7.3

$$p(i,i) = p(i-1,i-1) \overset{and}{-} (\rho_P C_P)_R \left[u(i,i) - u(i-1,i-1) \right]$$ 2.7.4

where

$$\left. \begin{array}{l} (\rho_P C_P)_R = \rho_P(i-1,i-1)\, C_P(i-1,i-1) \\ \overset{and}{(\rho_B C_B)_L = \rho_B(i,i-1),\, C_B(i,i-1)} \end{array} \right\}$$ 2.7.5

for the first approximation.

In the second approximation they are:

$$\begin{array}{l} (\rho_P C_P)_R = \rho_P(i-\tfrac{1}{2},i-\tfrac{1}{2}) \cdot C_P(i-\tfrac{1}{2},i-\tfrac{1}{2}) \\ \overset{and}{(\rho_B C_B)_R = \rho_B(i,i-\tfrac{1}{2}) \cdot C_B(i,i-\tfrac{1}{2})} \end{array}$$ 2.7.6

Knowing p (i, i) thermodynamic conditions on both sides of the contact front can be found through the respective isentropes and the continuity of pressure across the contact front.

The location of the point (i, i) is simply determined from the condition that the front moves at the local particle velocity and the intersection of the left running characteristic at (i, i) as follows:

$$t(i,i) = \frac{\{uc \cdot t(i-1,i-1) - x(i-1,i-1)\} - \{t(i,i-1) - x(i,i-1)\}}{(uc - cL)}$$

2.7.7

and

$$x(i,i) = x(i-1,i-1) + uc\left[t(i,i) - t(i-1,i-1)\right] \qquad 2.7.8$$

where $\quad uc = u\left(i-\tfrac{1}{2}, i-\tfrac{1}{2}\right)$

and $\quad CL = u\left(i, i-\tfrac{1}{2}\right) - C_B\left(i, i-\tfrac{1}{2}\right) \qquad 2.7.9$

where the second approximation is used with no

iteration being necessary.

Having determined the next point on the contact

front, points along the line JJ = i can then be

determined using the method of Section 2.5. In this

manner the whole region can be solved and the

transmitted wave although not centered any more is

still simple and the interaction problem can be

handled as previously, with point (x_B, t_B) being

replaced by the corresponding (x (i), t (i)) for

I = JJ (i.e., points on the contact front)

2.8 Calculation of the Isentropes and Several Approximations

In the previous section, we have assumed the functions $\rho = \rho_{is}(p)$ and $c = c_{is}(p)$ along the isentropes as known. They may be obtained by considering the second law of thermodynamics in differential form.

$$T\,dS = dE + p\,d\left(\frac{1}{\rho}\right)$$

$$2.8.1$$

For an isentropic process this reduces to

$$dE = -p\,d\left(\frac{1}{\rho}\right) = \frac{p}{\rho^2}\,d\rho$$

or integrating

$$E = \int \frac{p}{\rho^2}\,d\rho \qquad\qquad 2.8.2$$

Substituting equation 2.8.2 into the equation of state 1.3.7 and 1.3.8 and numerically integrating the isentropes can be obtained.

Several aluminum isentropes have been plotted in Fig. 5 along with the Hugoniot curve calculated from equation 1.3.7. Note that as the material is more strongly shocked, the isentropic expansion becomes more and more like that of a gas (i.e. $\rho \longrightarrow o$ and $p \longrightarrow o$). The experimental points of Walsh (Ref. 1) and Al'tshuler (Ref. 6) are also given showing excellent agreement.

46

FIG. 5 ALUMINUM HUGONIOT AND ISENTROPES
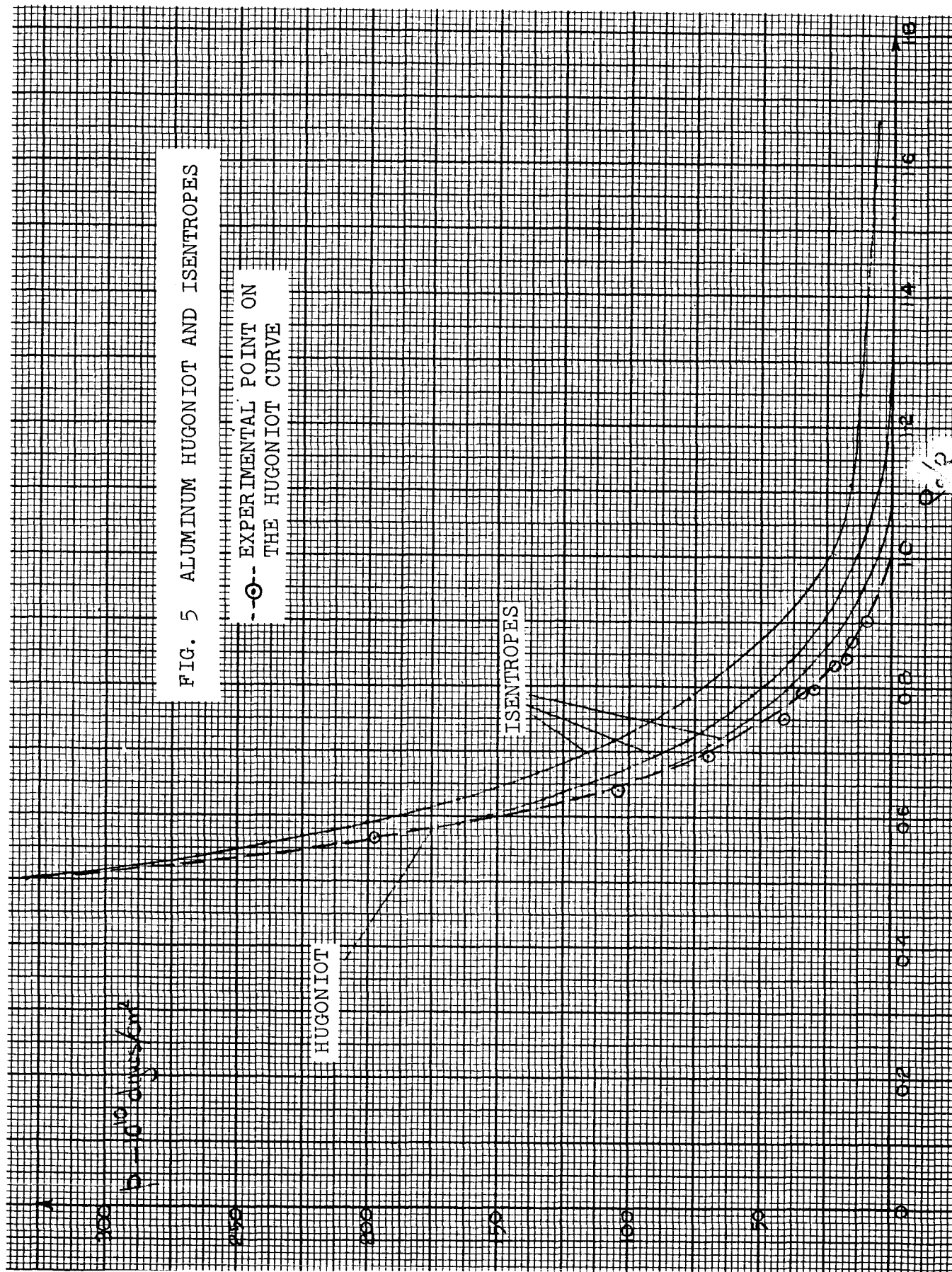
There are several approximate equations for
solid isentropes. One of the most widely used is
Murnaghan's (Ref. 23).

$$p = A_m \left[\left(\frac{\rho}{\rho_o} \right)^{\gamma_m} - B_m \right]$$

2.8.3

This equation is based on the theory of finite strain
and shows good qualitative agreement with metal
behaviour and with condensed states in general.
Chou at al. (Ref. 18) has tabulated the constants
A_m, γ_m, and B_m for various shock strengths in
aluminum. He obtained these constants by fitting
equation 2.8.3 to isentropes calculated from
Tillotson's equations (equations 1.3.7 and 1.3.8).
Comparison of equation 2.8.3 with the more accurate
isentropes shows good agreement throughout the
pressure range, with the best agreement shown for
the not so strongly shocked isentropes (Figs. 6 & 7).

As the material becomes more strongly shocked,
the constant $B_m \longrightarrow o$ and the material behaves more
and more like a gas. When $B_m = o$, equation 2.8.3
becomes the ideal gas equation for an isentrope

$$p = A_{id} \left(\frac{\rho}{\rho_o} \right)^{\gamma_{id}}$$

2.8.4

The constant γ_{id} is found from the initial shocked
state as follows:

FIG. 6 ALUMINUM ISENTROPE CORRESPONDING TO A IMPACT VELOCITY OF 10.07 KM/SEC

49

FIG. 7   ALUMINUM ISENTROPE CORRESPONDING
TO A IMPACT VELOCITY OF 15.67 KM/SEC
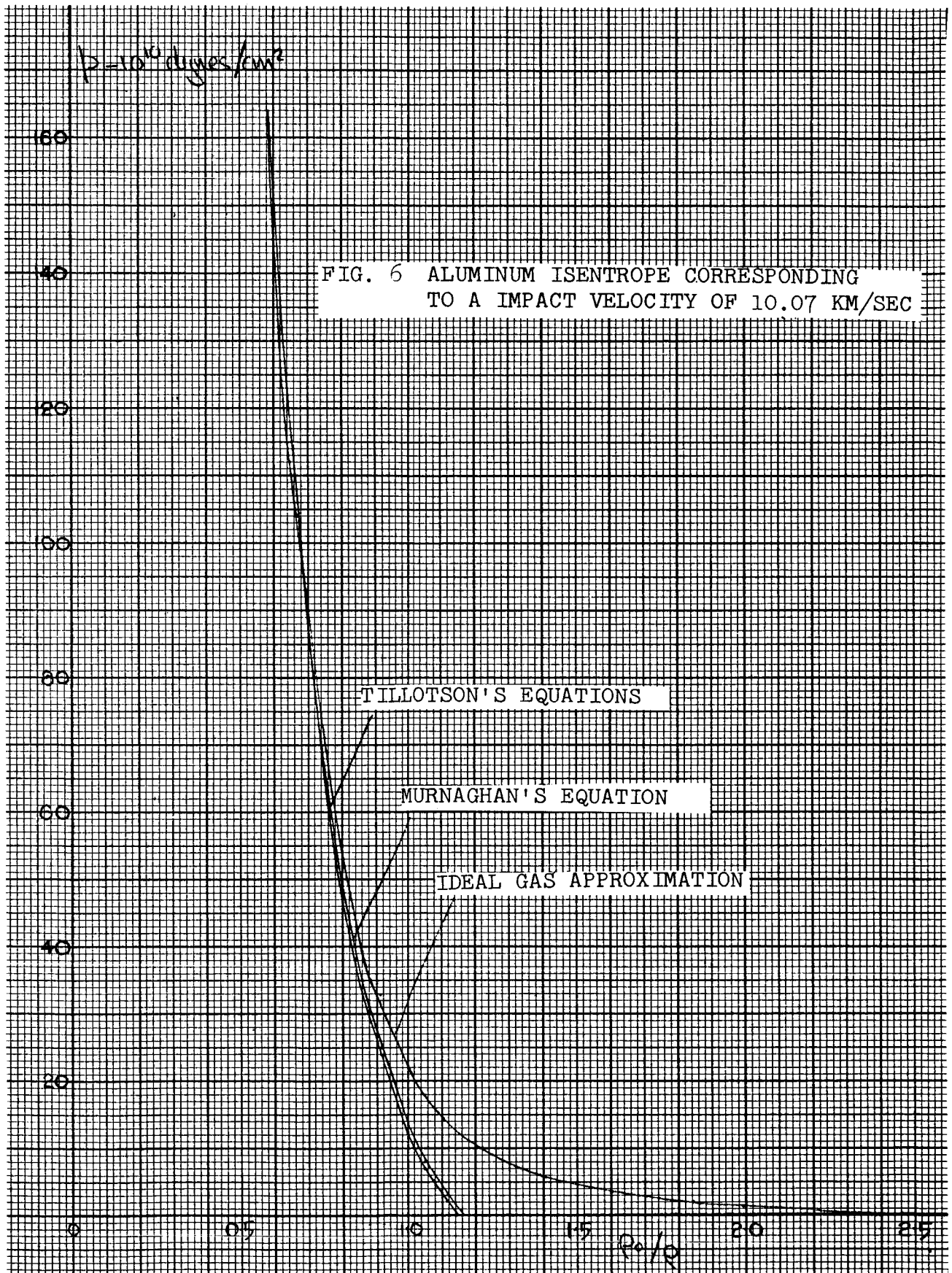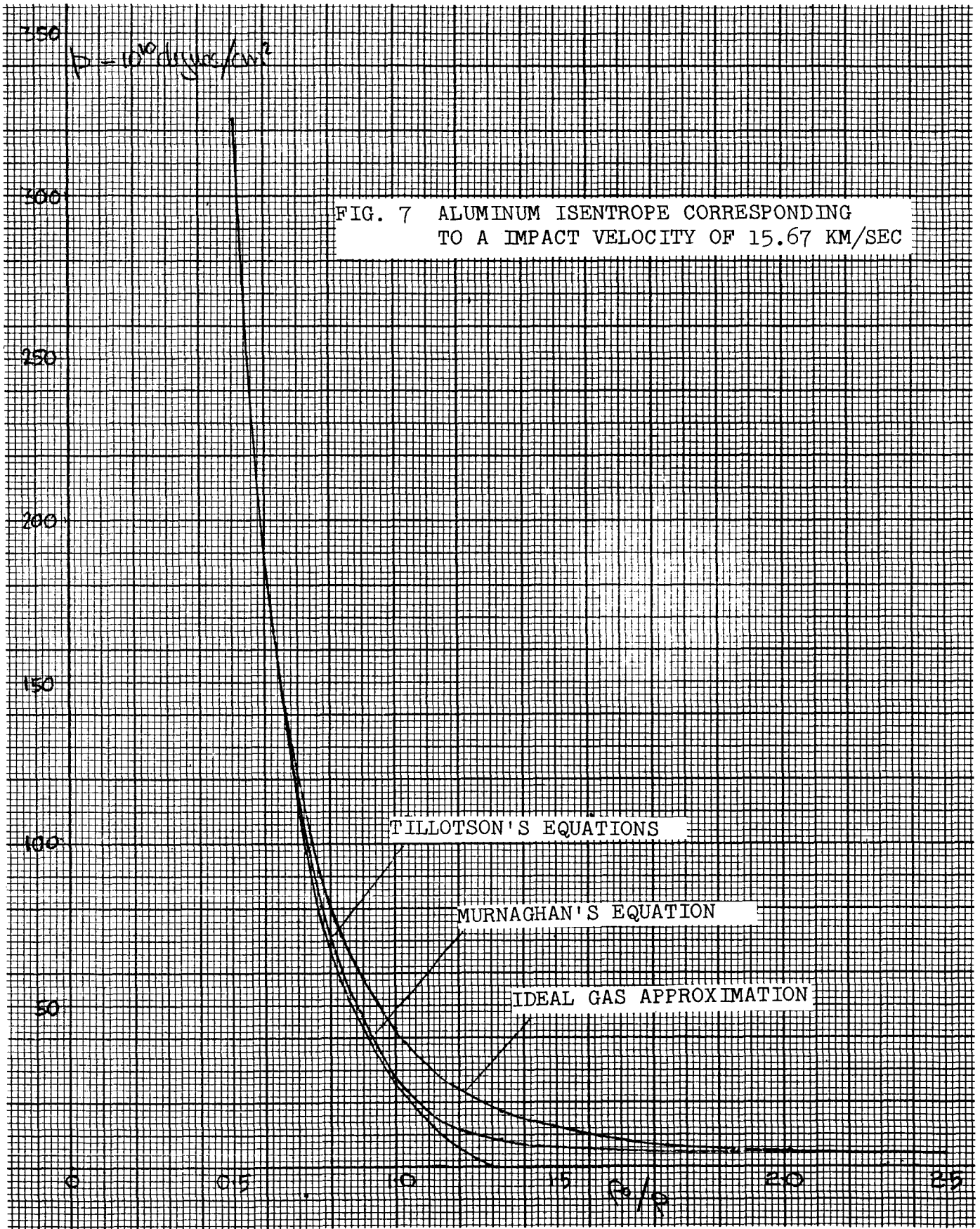
i.e., for an ideal gas

$$E = \frac{1}{\gamma_{id}-1} \frac{p}{\rho}$$

therefore $\gamma_{id} = 1 + \frac{p}{E\rho}$ evaluated

at a point on the Hugoniot.

A_{id} is calculated from the initial shocked state.

Comparison of equation 2.8.4 with equation 2.8.3 and the numerically integrated isentropes shows surprisingly good agreement for reasonably high pressures (above 1/4 x shock pressure).

For computer calculations relatively little is gained by using these simpler forms, since either Tillotson's equations directly or curve fits to the isentropes can be used quite readily. The importance of such simple forms as equations 2.8.3 and 2.8.4 lies in the fact that closed solutions can quite often be obtained with the resulting insight on how the various parameters affect the problem.

3. RESULTS AND DISCUSSIONS

3.1 Initial States

The strong shock system initially formed on impact can nearly always be represented by a one-dimensional formulation unless the impact geometry is unusual (e.g. a cone impacting vertex first). Therefore, the shock system considered in Section 2.3 has general application to the entire hypervelocity impact problem.

In solving the system of equations or Section 2.3, the initial pressure p_O was neglected with respect to the shocked pressure. The experimental Hugoniot curves reported in Ref. 6 were used. They represent best fit data of all experimental work to date and have an accuracy of approximately $\pm$ 1% of the shock pressure. One drawback is using such information is that it cannot be extrapolated much beyond the range of the experimental data and therefore, the calculations are limited to below 15 km/sec. impact velocity.

The equations were then solved using an iterative technique (Newton-Raphson method) for the shock parameters p, ρ , E, u, and ω as a function of the impact velocity V. The results are plotted in Figs. 8 - 11 for the impact of aluminum on copper, lead and aluminum. These results correspond closely to the ones published by Maiden (Ref. 16) which is

52

FIG. 8   PELLET SHOCK DENSITY RATIO
VERSUS IMPACT VELOCITY

53

FIG. 9   PRESSURE BEHIND BOTH PELLET AND
         BUMPER SHOCKS VERSUS IMPACT VELOCITY

54

FIG. 10   PELLET SHOCK VELOCITY
VERSUS IMPACT VELOCITY

FIG. 11 .BUMPER PARTICLE VELOCITY
VERSUS IMPACT VELOCITY
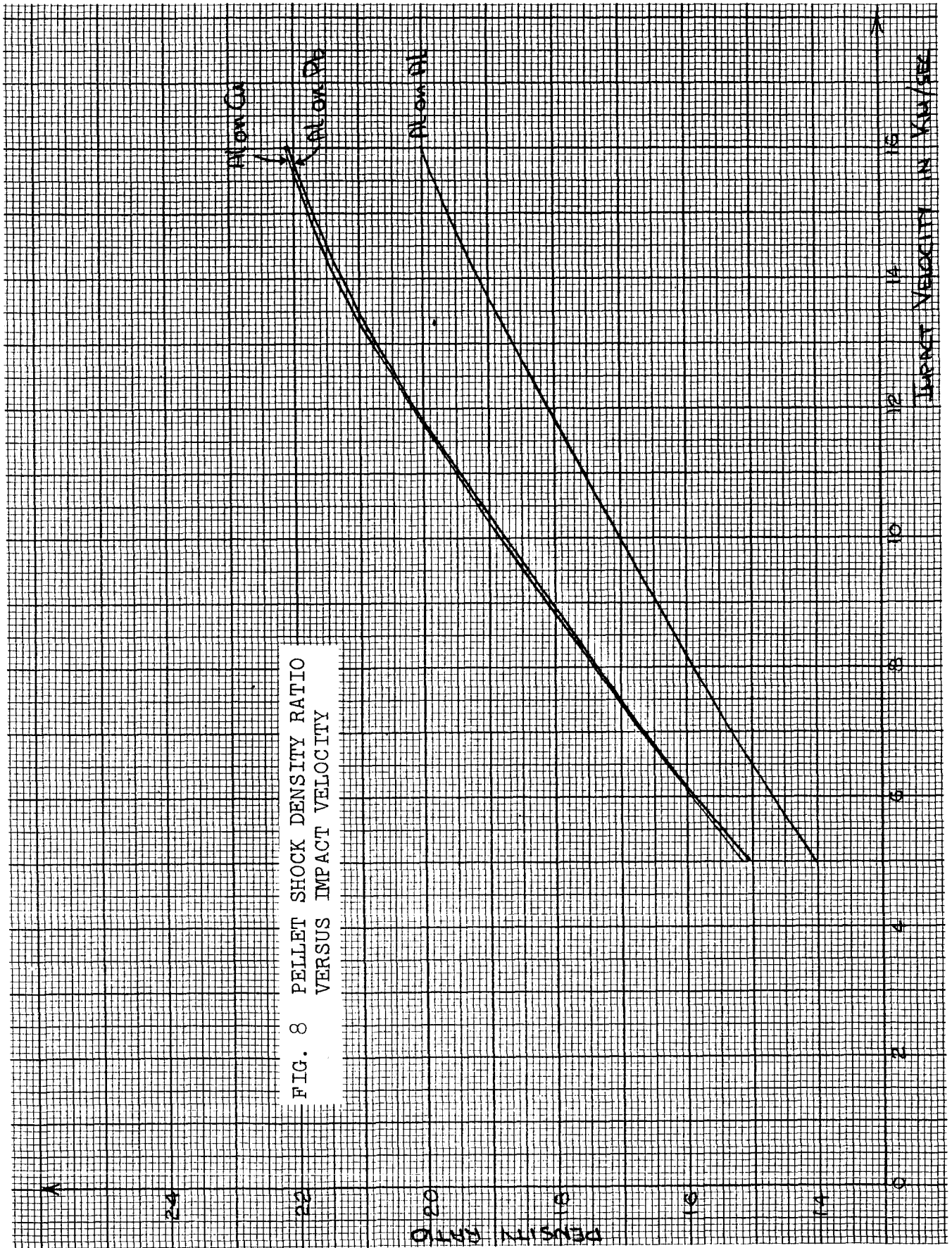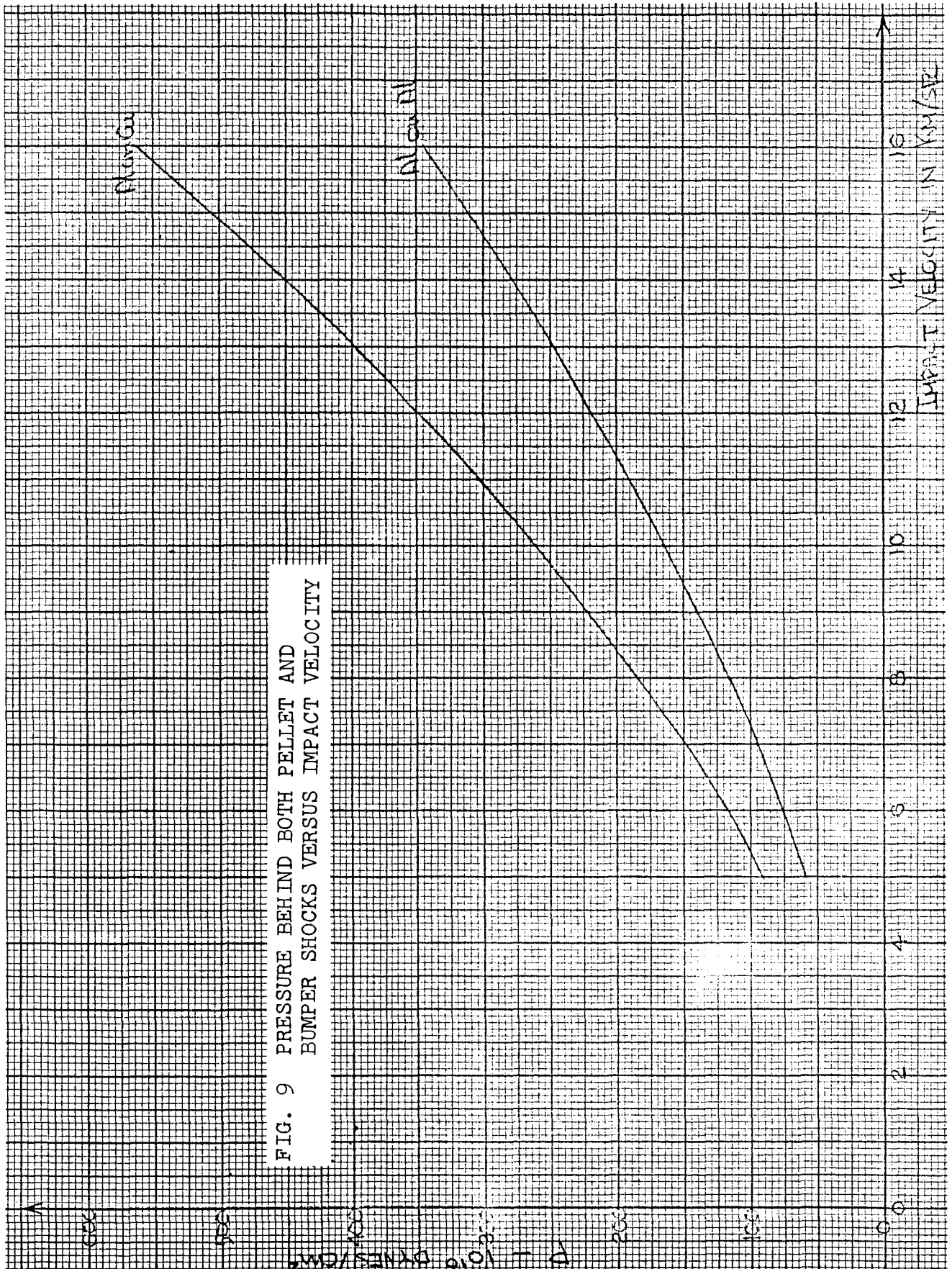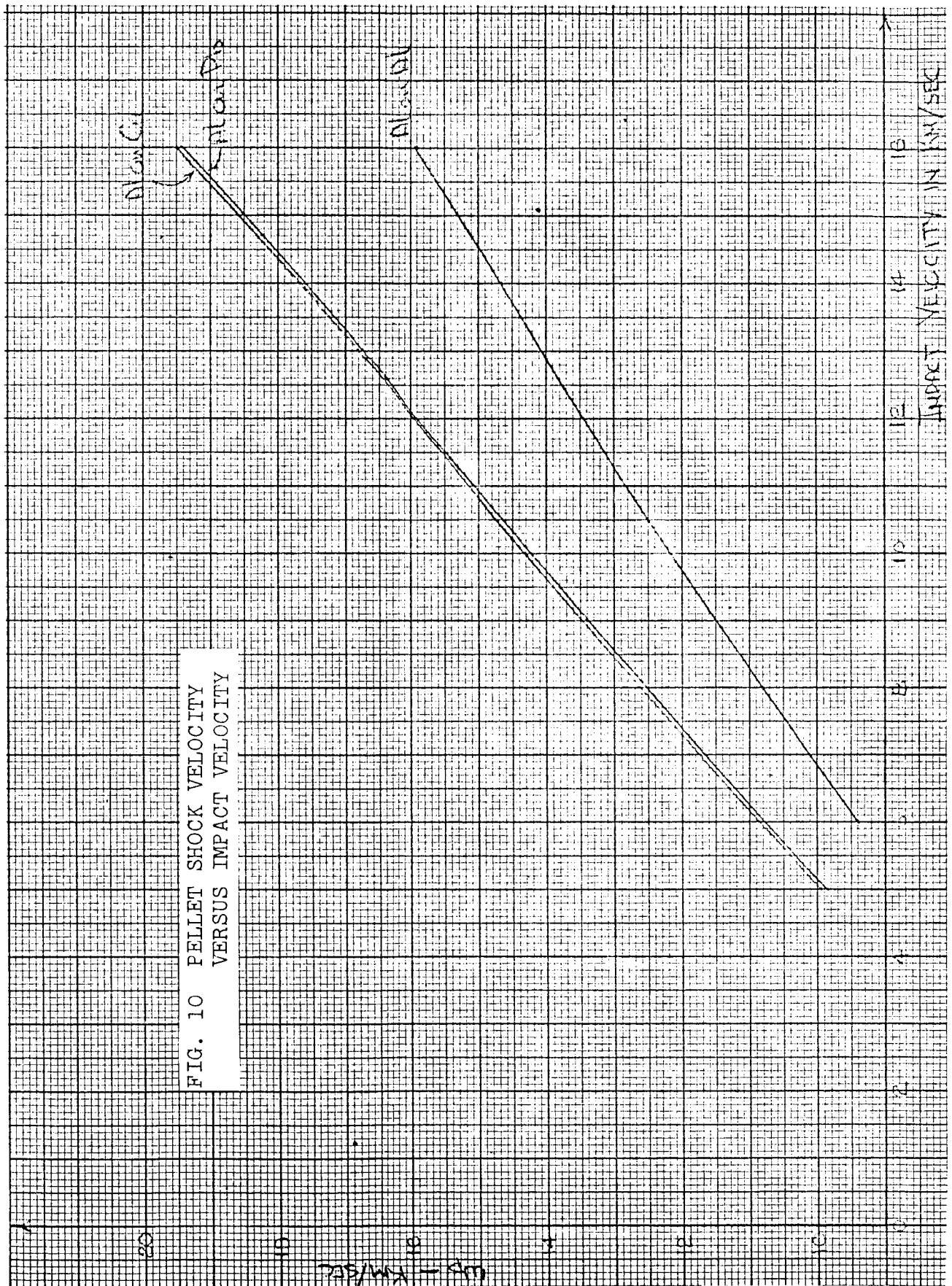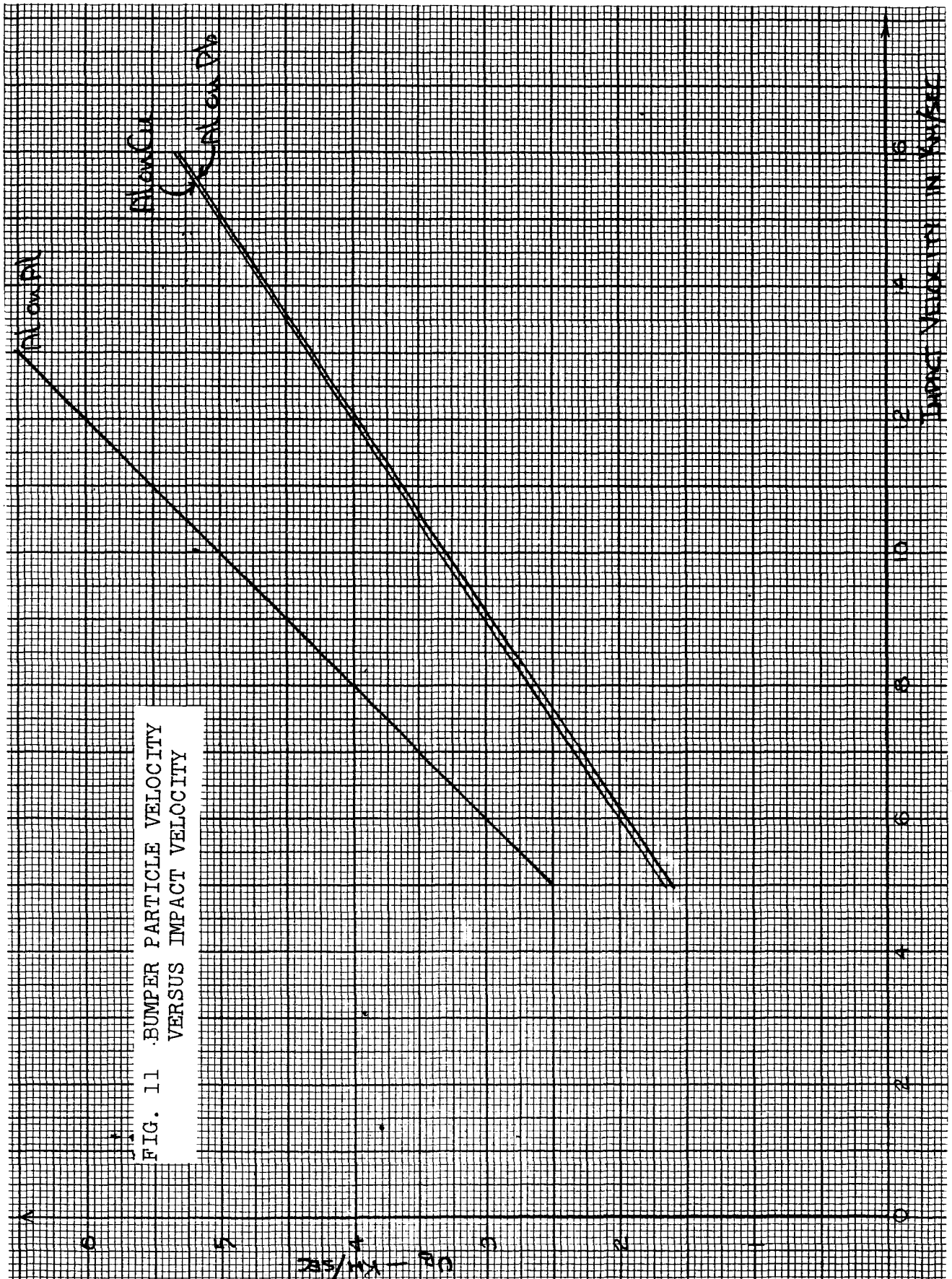
not surprising since the same experimental data was used in both cases. For a more exhaustive coverage of material combinations the reader is referred to Maiden's work where the impact of aluminum on magnesium, aluminum, titanium and gold is considered.

The general trend is clear. As the bumper material increases in density, the pellet material is more strongly shocked for the same impact velocity and at the same time the particle velocity behind the bumper shock is reduced. In other words a denser bumper is more effective in reducing the resultant velocity of the system and in the process converts this kinetic energy into higher thermo-dynamic states.

In addition, nearly linear relations hold for the variation of the velocities u, and w with impact velocity. This curious fact has been noted in the experimental determination of shock Hugoniots and no truly satisfactory explanation has been advanced for this phenomenon at this date (Ref. 8)

Many of the effects observed here had been explained qualitatively in earlier reports (Refs. 13 and 14) using the ideal gas approximation. For example the behaviour of the impact of different materials can best be examined by looking at the behaviour of the bumper particle velocity, u_B.

The relation derived in Ref. 13 for u_B is:

$$u_B = \cfrac{V}{1 + \sqrt{\cfrac{\gamma_B + 1}{\delta_P + 1}, \cfrac{\rho_{Bo}}{\rho_{P_o}}}}$$

3.1.1

Under the ideal gas assumption, the ratio $\dfrac{\gamma_B + 1}{\gamma_P + 1}$

is a constant. Therefore, we plot $\sqrt{\dfrac{\delta_B + 1}{\delta_P + 1} \dfrac{\rho_B}{\rho_o}}$

versus impact velocity V for the case of aluminum on

copper impact in Fig. 11-A. Although the function

oscillates slowly as impact velocity increases, its

value remains practically constant within narrow

limits. This oscillation can be explained as due to

the original curve-fitting of experimental data.

We can therefore say that although γ is in

general a function of the density ρ , or indirectly

of the impact velocity V, the variation for two

different materials is sufficiently alike for the

ratio $\dfrac{\gamma_B + 1}{\gamma_P + 1}$ to remain essentially constant.

The speed of sound in the shocked states was

also calculated from the Russian experimental data

(Ref. 7, see TABLE II). The results are plotted in

Figures 12 and 13, for the various material

combinations.

In comparing these values to the ideal gas

approximation, an inconsistency arises. Using the

strong shock approximation, the density ratio for

an ideal gas becomes:

$$\rho / \rho_0 = \frac{\gamma + 1}{\gamma - 1}$$

3.1.2

FIG. 11-A VARIATION OF $\sqrt{\dfrac{\delta_g+1}{\delta_p+1}\cdot\dfrac{\rho_g}{\rho_p}}$ WITH IMPACT VELOCITY
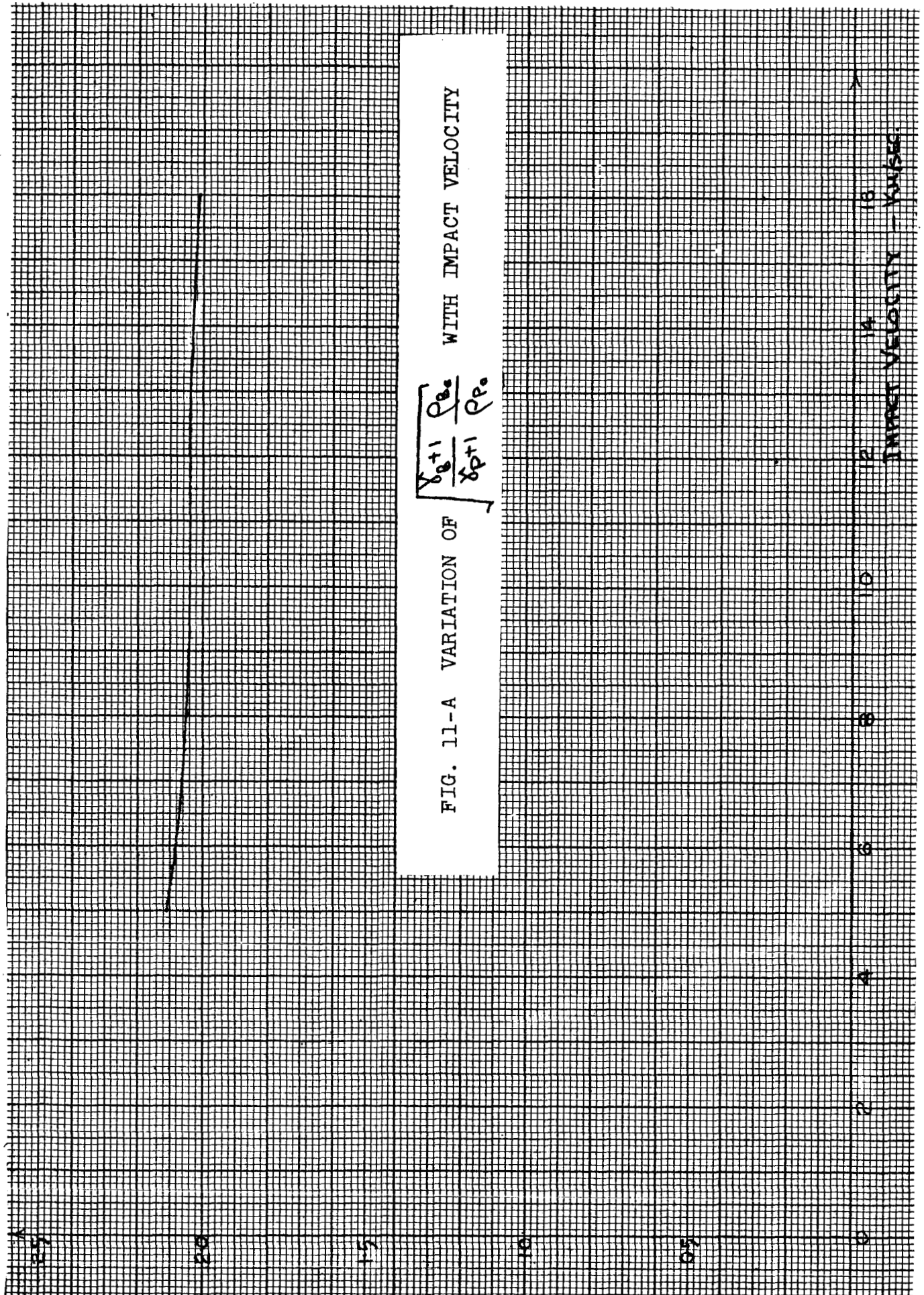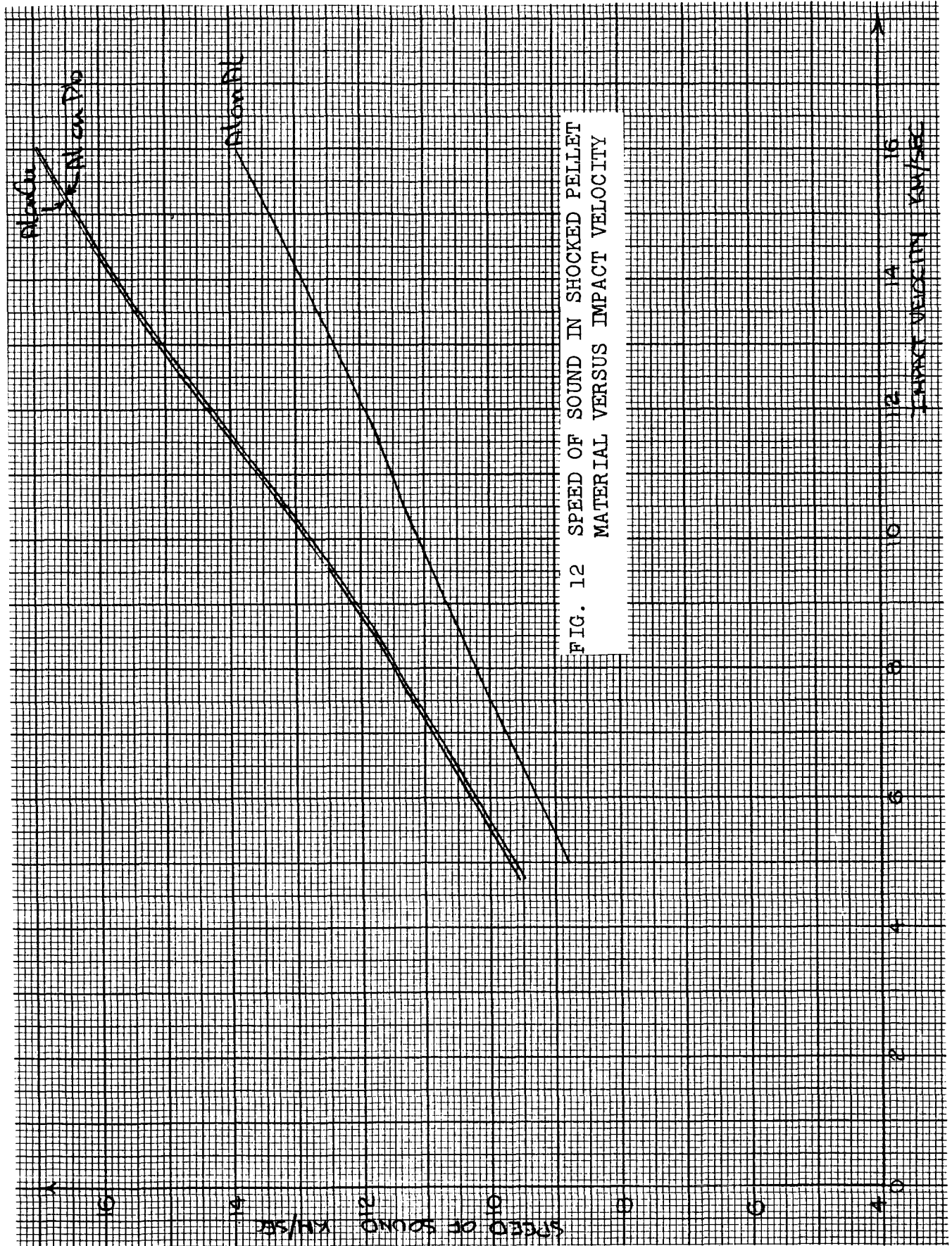
FIG. 12 SPEED OF SOUND IN SHOCKED PELLET
MATERIAL VERSUS IMPACT VELOCITY

FIG. 13 SPEED OF SOUND IN SHOCKED BUMPER
MATERIAL VERSUS IMPACT VELOCITY
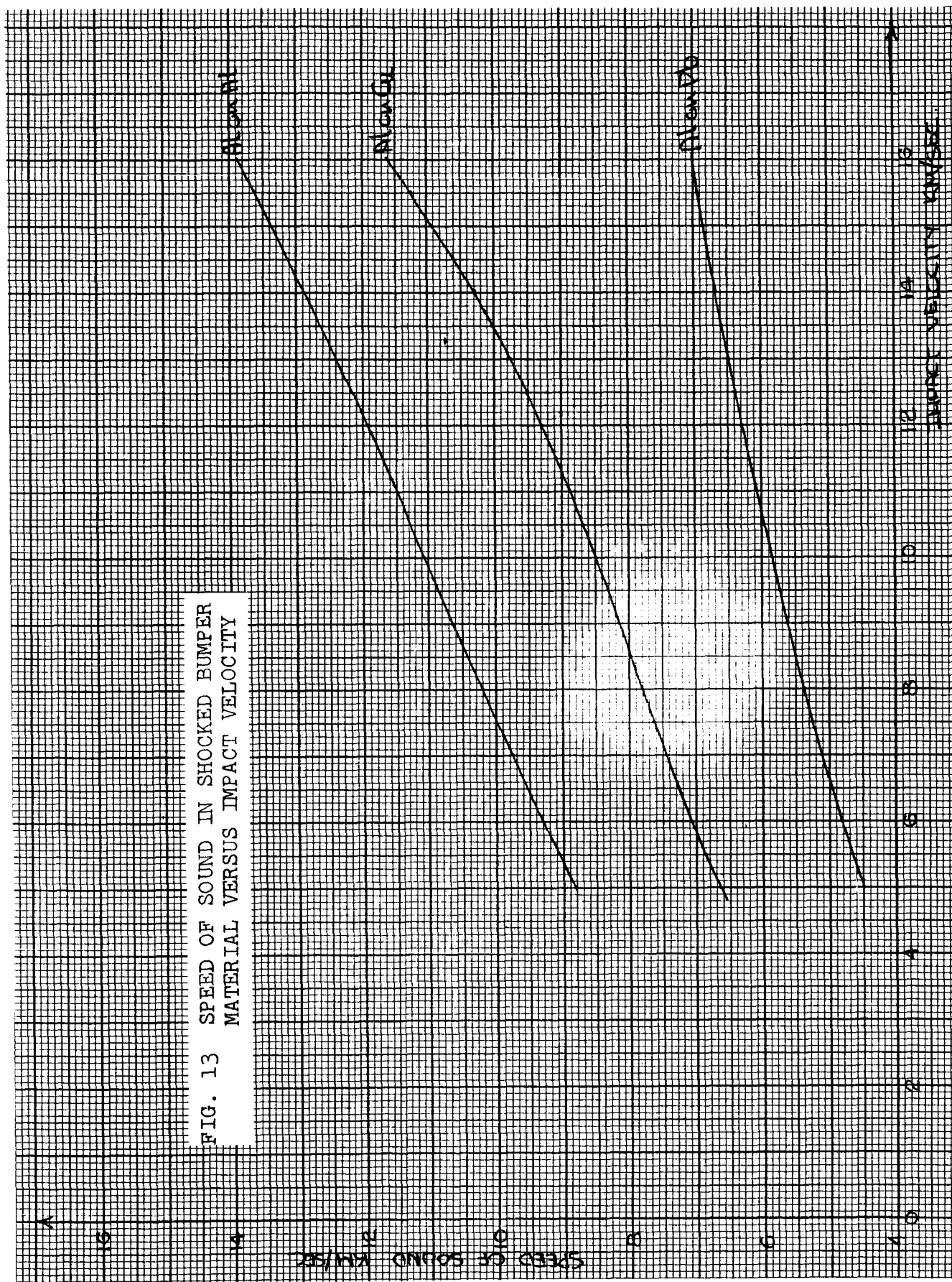
Also, for an ideal gas the speed of sound is given by:

$$C^2 = \frac{\gamma p}{\rho}$$

3.1.3

where both γ's are the same in a self-consistent theory. From the experimental data, however, it is found that separate determinations of γ from equations 3.1.2 and 3.1.3 differ by as much as 30% with the γ from equation 3.1.3 being always lower.

The obvious explanation would be to say that the material does not behave as an ideal gas and we have therefore no reason to expect a consistency. There is however, a more fundamental reason for this discrepancy. In determining γ from the shock density ratio we are considering a transition from unshocked states to final shocked states. The γ calculated in this manner is representative of the whole range and is an average value. The second determination considers only the final shocked state and is therefore only representative of this final state.

This view is supported by the fact that isentropes calculated by using the γ from equation 3.1.2 agree surprisingly well with more exact determinations as in section 2.8.

3.2 Interaction Points

A natural development of the calculation of the initial states is the location of the point where the rarefaction waves first interact, marking the disappearance of the region of constant properties existing behind the shocks.

This calculation as described in section 2.4 introduces the geometry of the one-dimensional impact i.e. pellet and bumper lengths) and we can thus study the interrelated effects of velocity and bumper plate thickness.

Since the results can be scaled all calculations, here and subsequent to this section, have been performed for a standard 10 mm long aluminum pellet. In Figs. 2, 3, 4, the location of the interaction point (x_i, t_i) is plotted as a function of impact velocity and bumper thickness for the impact of aluminum on aluminum, copper and lead respectively.

As can be seen from the graphs, both impact velocity and bumper plate thickness greatly influence the point of interaction. Both an increase in impact velocity and bumper thickness tend to drive the interaction point further to the right (towards positive x).

A change in bumper material also causes
important change as can be seen by comparing
Figs. 2 & 4. The bumper thickness seems to become
a much more important parameter as the bumper density
is increased, with impact velocity having a decreased
importance except in determining the time of inter-
action.

Another important fact is that these graphs point
out the location of the pellet shock. For most
impacts in the experimental range, $W_p >$ V, meaning
that the pellet shock lies ahead of the bumper
(negative x). The broken line shows the points
(x_p, t_p) where the pellet shock first reaches the
pellet free-surface, which of course is the furthest
point the pellet shock will ever reach. An increase
in impact velocity is seen to bring the shock closer
to the bumper until for an impact velocity of 15.5
km/sec the shock lies right on the bumper for
aluminum on aluminum impact. For denser bumper
materials the shock lies even further from the bumper
at the same velocity. The position of the pellet
shock has a great effect in determining upstream flow
(negative x) especially radial flow effects for finite
diameter pellets. Radial effects are of course
excluded in our one-dimensional analysis but cannot be
neglected for pellets of finite diameter, even at very
short times after impact.

3.3 The Interaction Region

3.3.1 Accuracy of the Numerical Techniques

The calculation procedure outlined in Section 2.5, 2.6 and 2.7 was used to write a computer program in the Fortran coding system for an IBM 7040 digital computer. The calculation of the initial states (as in Sections 2.3 and 2.4) was included in this program so that only the impact velocity, bumper thickness and properties of the materials had to be fed into the program as the variable parameters.

In specifying the grid size, the method introduced in Section 2.6 was used (equation 2.6.1) $\triangle$ p was set equal to $-p_s/100$ in almost all cases calculated where p_s is the initial shock pressure. This interval size was found to give stable and accurate results up to times after impact of about 2.5μ sec. for a standard 10 mm long pellet. At times greater than about 3μ sec. the mesh size diverged and the finite difference procedure became unstable.

The accuracy and stability of the program were checked by comparing the results to several exact solutions given by Stanyuokovich (ref. 17) for the interaction of rarefaction waves using the special case of an ideal gas with $\gamma = 3$. The results agreed within $\pm 1\%$ for times less than 2.5μ sec. after which the answers became increasingly inaccurate.

Since a one-dimensional analysis is only valid for short times after impact, an improvement of the long term performance of the program was not attempted.

3.3.2 Effect of Equation of State on Expansion

After noting the surprisingly good agreement of the constant γ approximation at high pressures (Section 2.8) it was decided to see if this agreement could be extended to calculations that included the dynamics of the problem.

Using as the "exact" isentrope a polynomial curve-fit to the numerically integrated Tillotson equation (see Section 2.8), the case of impact of aluminum on aluminum at 10.07 km/sec. was calculated. In the calculations whenever a negative pressure occurred it was set to zero. Negative pressures signify tensile stresses which could be permitted in a solid system, setting the negative pressure equal to zero signifies that the solid has yielded (dotted lines in Figs. 14, 16 and 17).

In Figs. 14 and 15, we show the density and pressure profiles respectively at times t_I, $t_I + 0.1$, and $t_I + 0.2$ after impact, where t_I is the time at which the rarefaction waves first start to interact.

FIG. 14   DENSITY PROFILE USING TILLOTSON'S EQUATION
IMPACT VELOCITY 10.07 KM/SEC, BUMPER THICK-
NESS IS 2.5 MM.

FIG. 15   PRESSURE PROFILES USING TILLOTSON'S EQUATION
IMPACT VELOCITY 10.07 KM/SEC, BUMPER THICK-
NESS IS 2.5 MM.
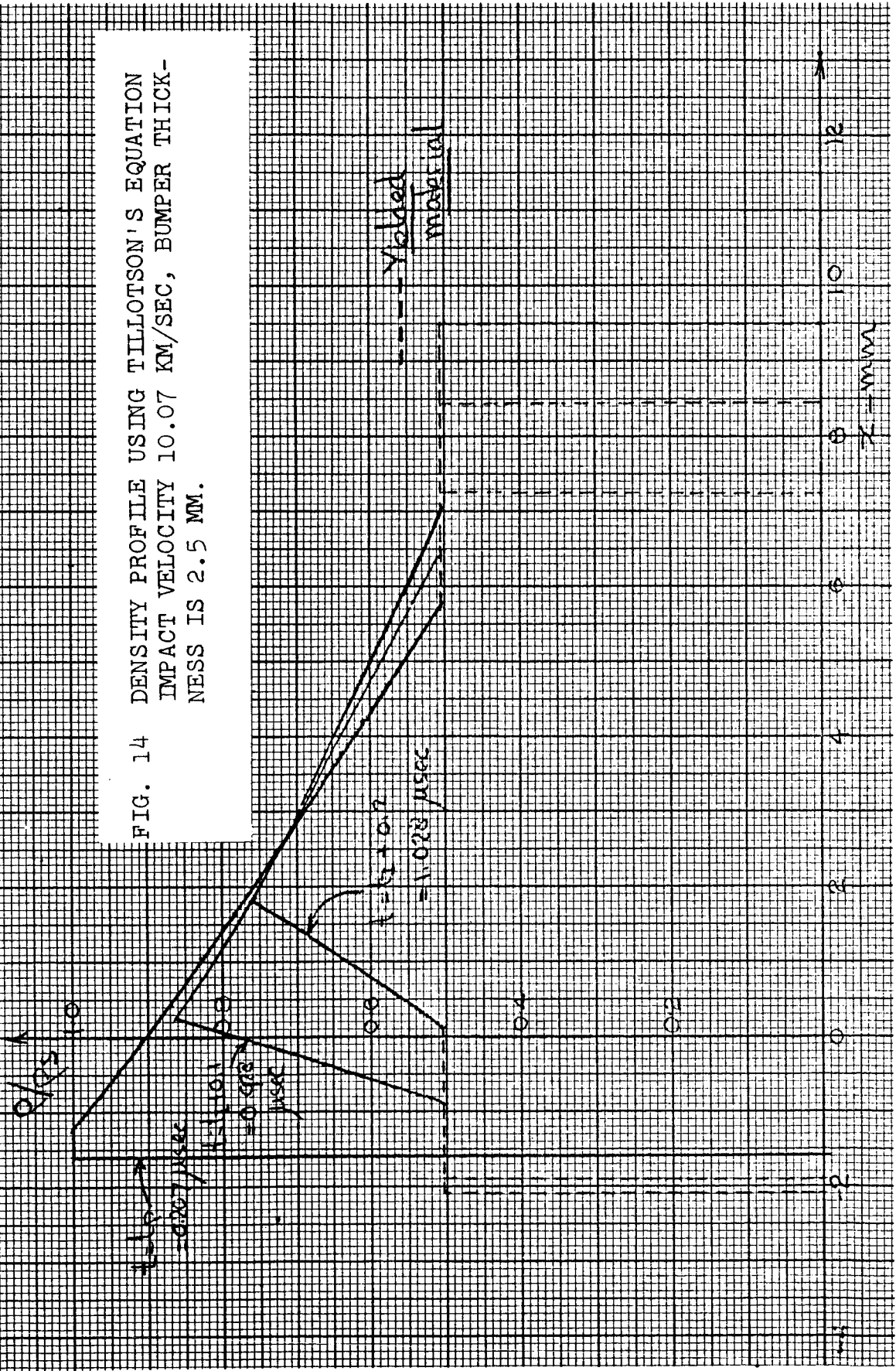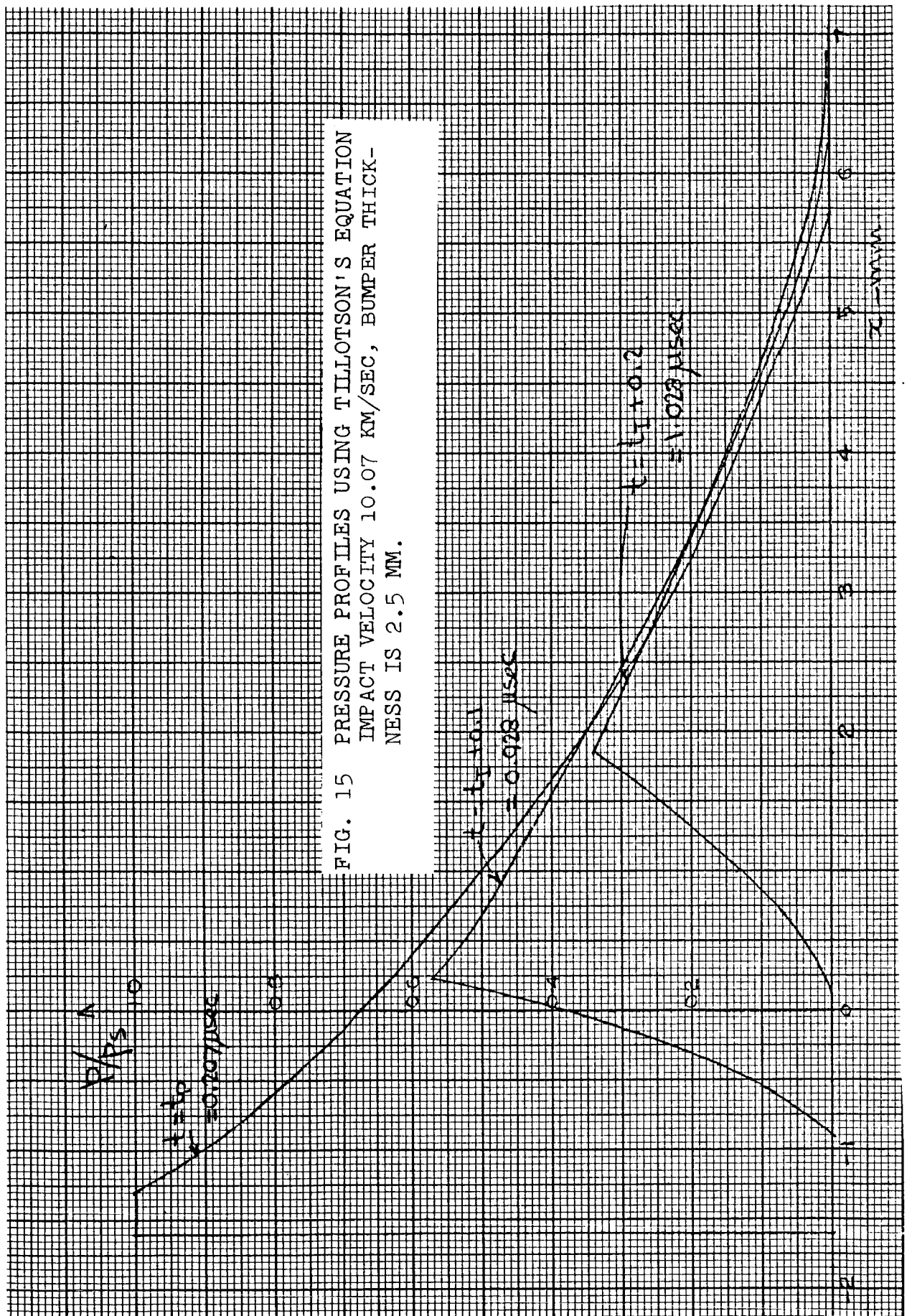
The graphs show a typical solid behaviour in that the density does not fall to zero at the escape front and also a rather rapid relaxation of static pressure of the material.

The above case was now recalculated using the same initial conditions but using a polytropic gas law calculated according to equations 2.8.4 and 3.1.2.

Figs. 16 and 17 give the density and pressure profiles respectively at time, $t_I + 0.1$ sec. for both the "exact" and "polytropic" case.

Both peak density and pressure are identical in both cases but the "polytropic" expansion has a shallower profile in the low pressure region. The big difference is the location of the escape fronts where pressure equals zero. For the "polytropic" gas the escape front lies far beyond those calculated using the more exact solution. However, long before the escape front is reached, the pressure has effectively dropped to zero (with respect to peak pressure) for the "polytropic" gas. Thus, the "effective escape front" where the first "observable" pressure occurs is much closer to the more exact solution than is indicated at a first glance when the "escape fronts" are compared.

FIG. 16 DENSITY PROFILE AT TIME $t = t_I + 0.1$ sec IMPACT VELOCITY 10.07 KM/SEC, BUMPER THICKNESS IS 2.5 MM.

FIG. 17 PRESSURE PROFILE AT TIME $t = t_I + 0.1$ sec IMPACT VELOCITY 10.07 KM/SEC, BUMPER THICKNESS IS 2.5 MM.
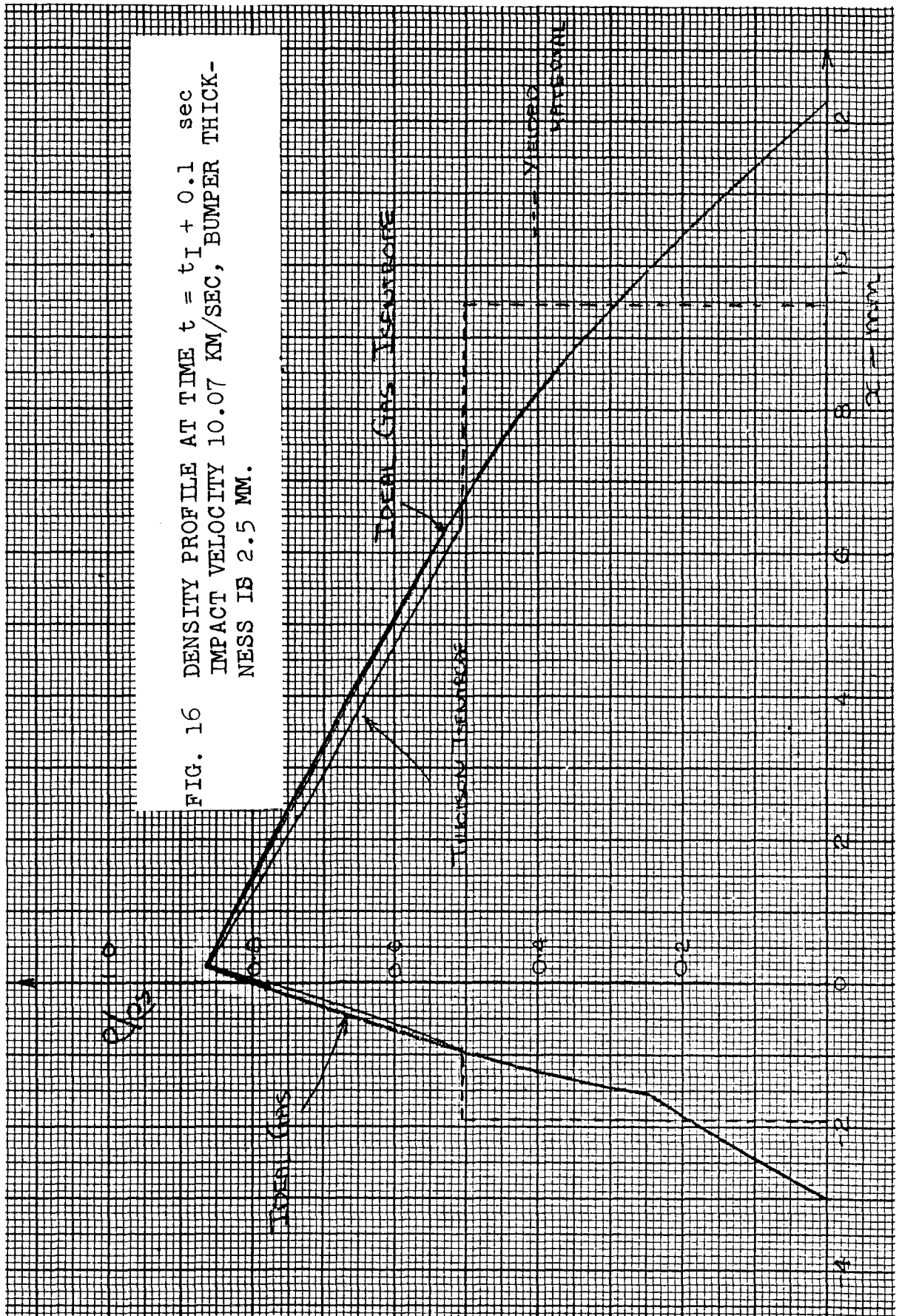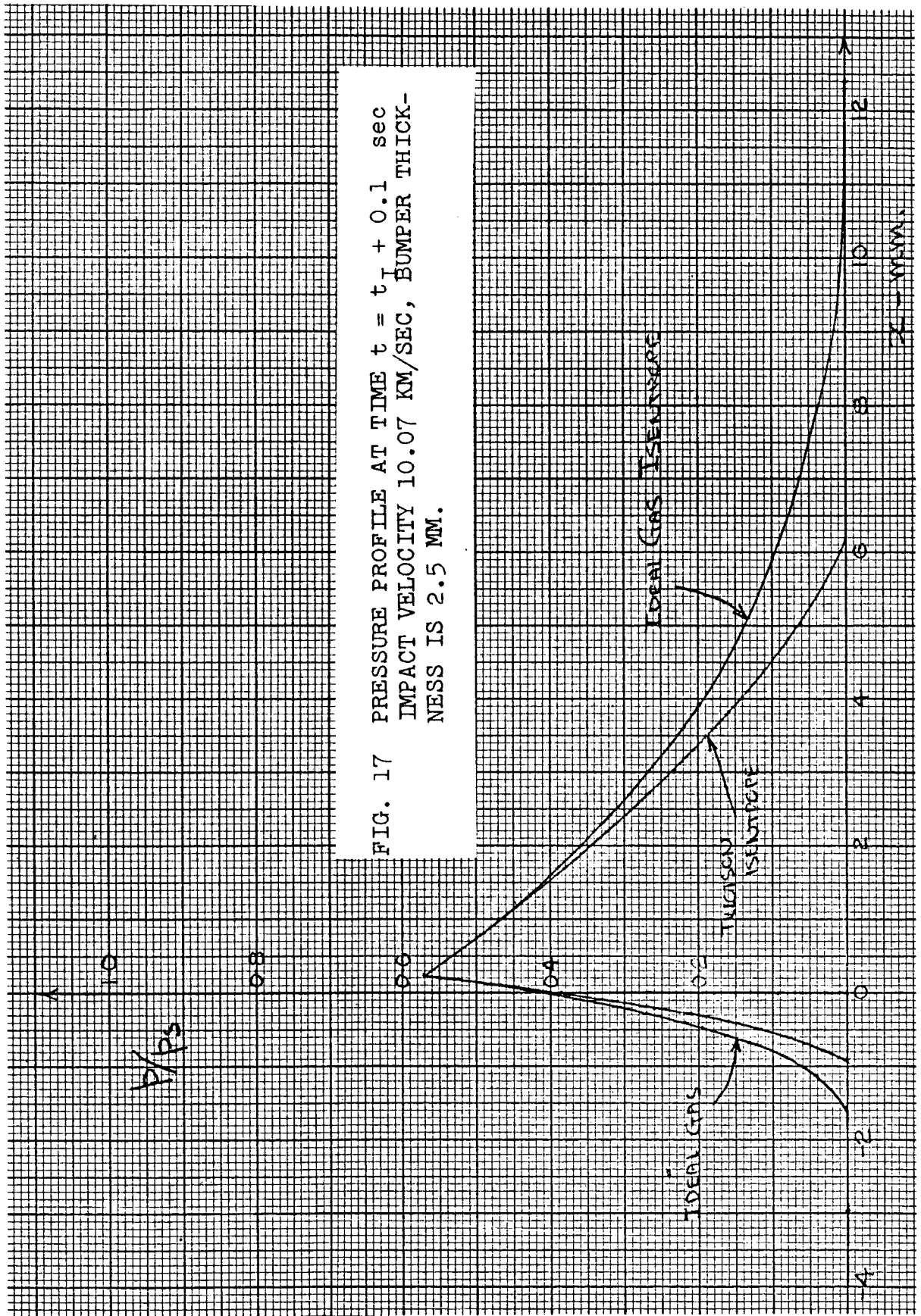
The case tested here is actually quite severe since the material was not shocked strongly enough to completely vapourize it. This resulted in a finite density at the escape front, which can of course, never be approached by a polytropic gas. Nevertheless, a satisfactory general agreement is noted with practically exact agreement in the high pressure region. As was shown in Section 2.8, the agreement between the polytropic gas laws and the more exact isentropes become much better in the low pressure region as the material becomes more strongly shocked.

3.3.3 Surface of Zero Velocity

The pellet escape wave generally moves with negative velocity (i.e. upstream) while the bumper escape wave moves in a positive direction (downstream). Somewhere in between these two extremes there must be a point of zero velocity. The determination of these points of zero velocity will then give an indication of the amount of flow that occurs upstream or downstream of the bumper.

In order to study the general behaviour of these surfaces of zero velocity as a function of impact velocity and bumper material, a series of cases were calculated using either aluminum or copper as bumper material at impact velocities varying from 5 - 15 km/sec.

FIG. 18 POINTS OF ZERO VELOCITY FOR
ALUMINUM ON ALUMINUM IMPACT
BUMPER THICKNESS IS 2.5 mm.

FIG. 19   POINTS OF ZERO VELOCITY FOR ALUMINUM ON COPPER IMPACT BUMPER THICKNESS IS 2.5 mm.
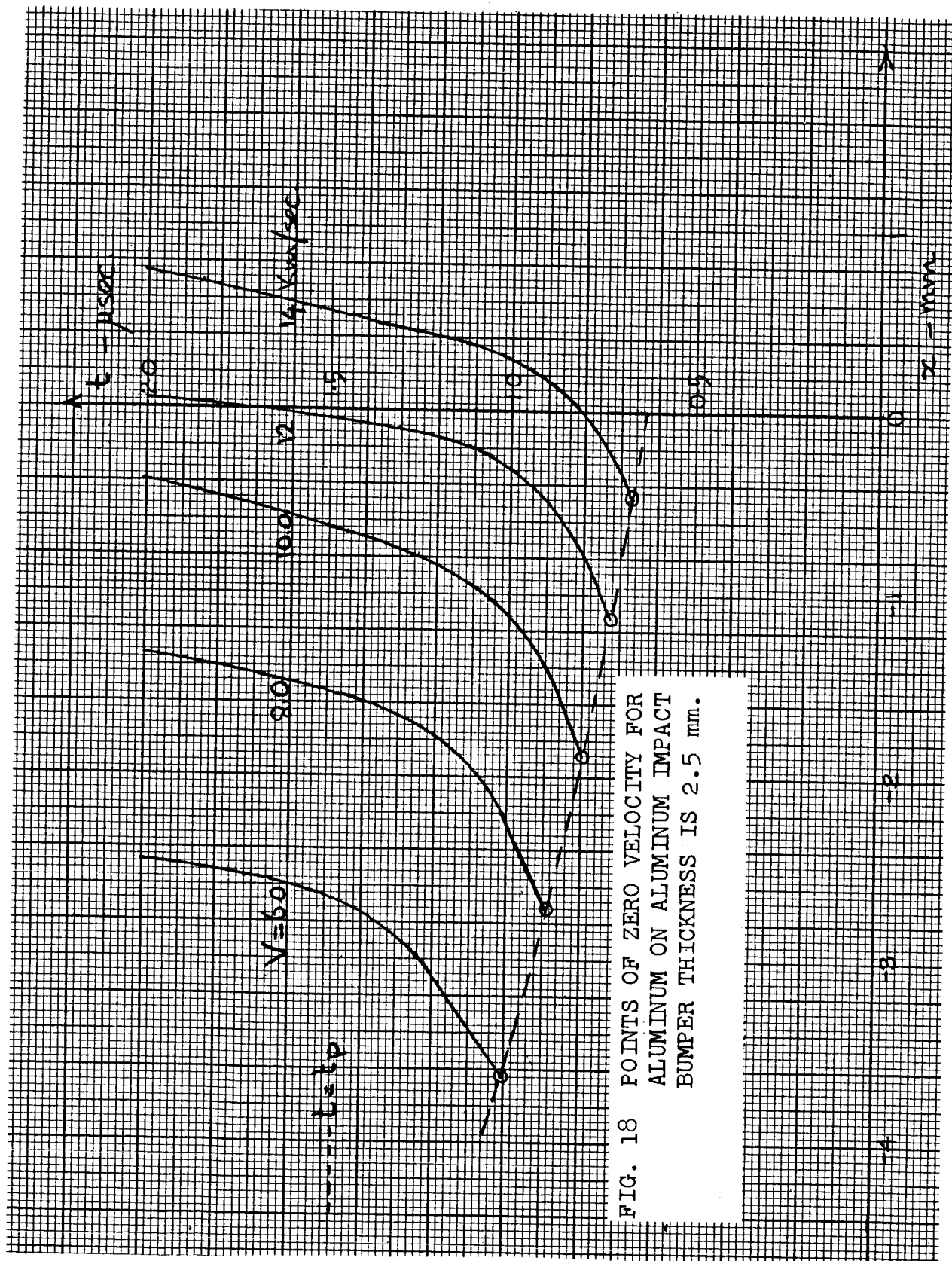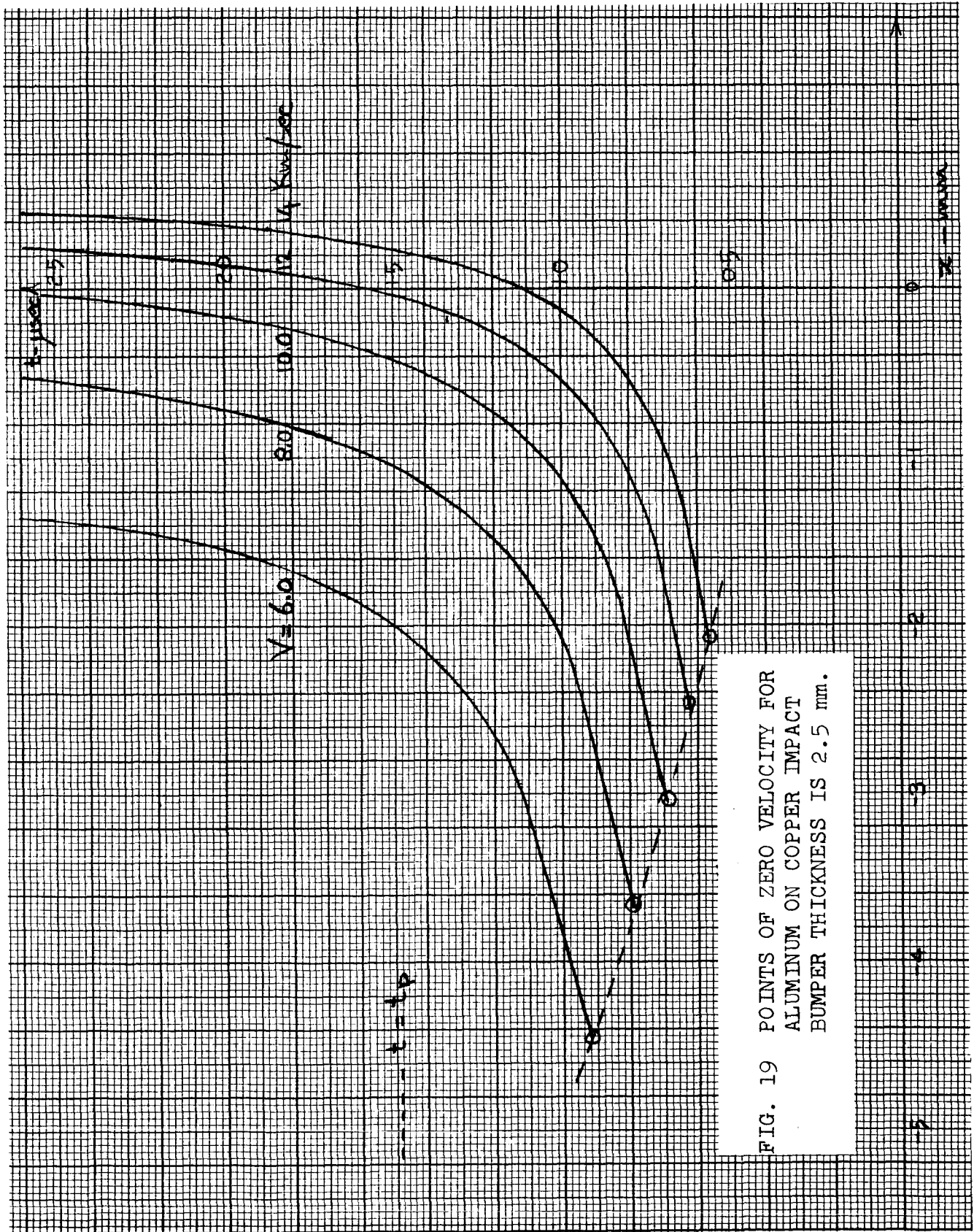
FIG. 20   COMPARISON OF EXACT SOLUTION OF CONTACT
FRONT WITH SOLUTION NEGLECTION NEGLECTING
REFLECTIONS.
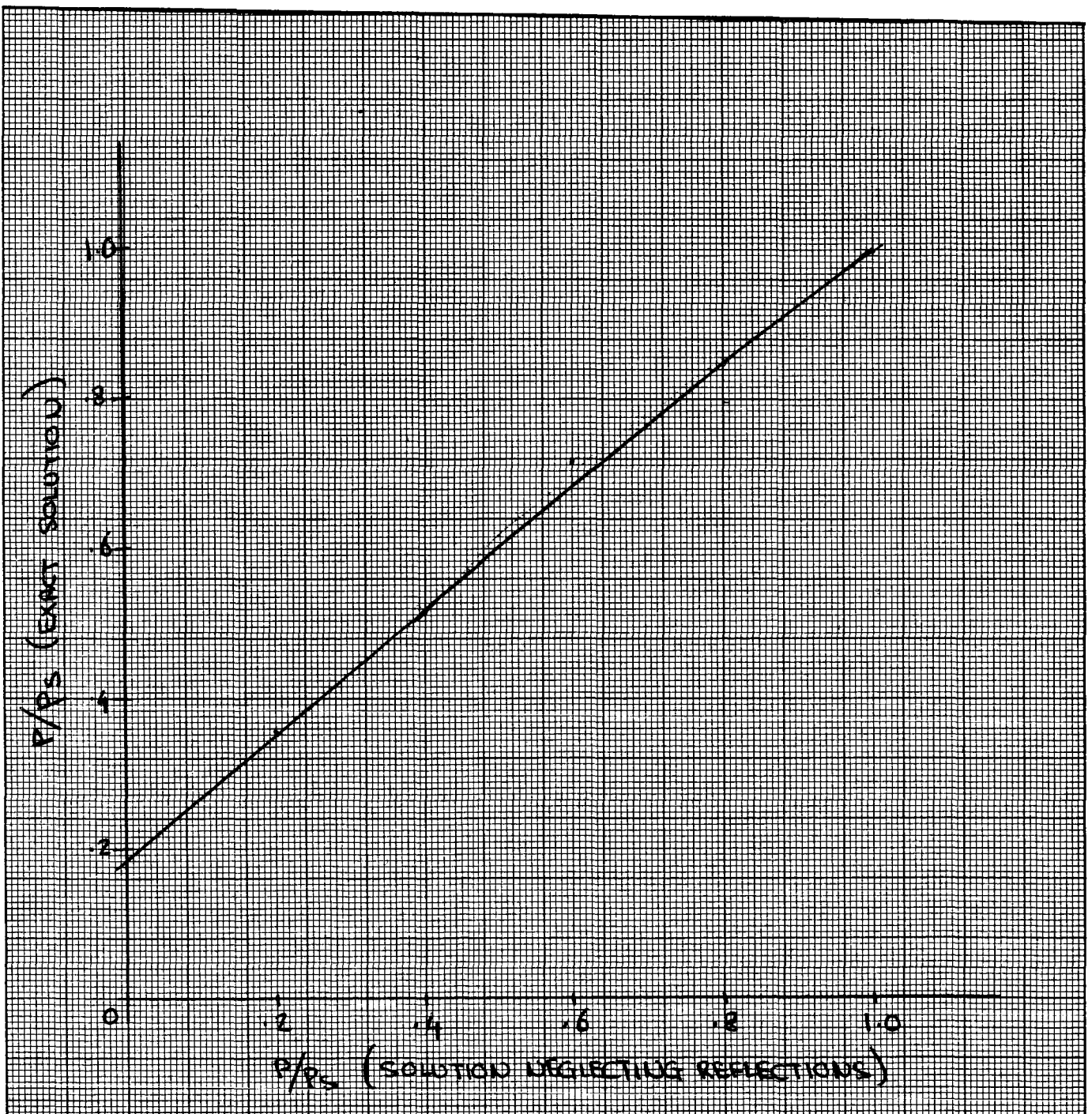
The initial states were calculated from
Al'tshuler's experimental data (TABLES I & II) and
the ideal gas approximation was used for the
expansion states. This last approach seemed
justified from the considerations of the previous
section and also of Section 2.8, especially at
impact velocities above 10 km/sec.

The results are presented in Figs. 18 & 19 for
aluminum on aluminum and copper impacts respectively.
A strong dependence of the zero velocity curves is
noted both on impact velocity and bumper material
(density), an increase in both tends to drive the
curves toward positive x while the general shape
tends to remain constant.

3.3.4 Reflections from the Contact Front

In some of the previous theoretical work (Ref.14)
the reflected waves from the contact front had been
assumed not to affect the incident rarefaction wave.

The calculations of the impact of dissimilar
materials show that this approximation although valid
near the points (x_c, t_c) where the rarefaction first
starts to interact with the contact front becomes
increasingly inaccurate as one progresses in time
along the contact front.

Fig. 20 compares the approximation to the
exact solution for the impact of aluminum on copper
at 10 km/sec. The approximation is seen to become
increasingly inaccurate as the pressure decays.

4. CONCLUSIONS

The following conclusions may be drawn from the foregoing theoretical analysis.

(a)   Useful theoretical predictions of the flow subsequent to impact may be made using a only one-dimensional model.

(b)   The upstream flow is strongly dependent on both bumper material and impact velocity.

(c)   A polytropic gas law provides a useful approximation of the expansion isentrope and gives qualitatively correct answers even when the material does not behave as a gas (i.e., is not vapourized).

(d)   From the calculation of various isentropes, it appears that for most common metals (aluminum, copper, iron) will not completely vaporize until impact velocities approaching 15 km/sec. are reached.

(e)   The expansion density profiles depend strongly on whether the material is vaporized or not, especially at the escape front.

(f)   Reflections from the contact front are important and have to be allowed in any analysis.

5. RECOMMENDATIONS FOR EXPERIMENTAL WORK

Three basic methods are available for experimental determination of the flow properties.

(a)   High speed photographic techniques including both single and multiple frames.

(b)   Flash X-ray absorption techniques.

(c)   Piezo-electric crystal pressure transducers.

All of the above systems can be obtained commercially giving sufficient time resolution (0.1 μ sec) for the impact phenomena to be observed.

Of the three methods the first two seem most applicable to the study of the initial expansion profile.

Some earlier framing camera shots were reproduced in Fig. 1. This technique can be extended to give 8 x 10^6 frames/sec. This then enables one to study shock position and initial expansion direction although the details of the one-dimensional regime are hidden.

Flash X-ray units can be obtained giving 7 x 10^{-8} sec. flash duration for as many as four channels. This enables one to study density gradients of the system. This seems to be the most promising approach and some of the work performed by Maiden (Ref. 16) indicates very good results.

Pressure measurements although essential in determining momentum flux of long term expansion have less application to the initial expansion.

APPENDIX A

THE METHOD OF CHARACTERISTICS FOR ONE-DIMENSIONAL UNSTEADY FLOW

The equations governing one-dimensional unsteady flow are readily deduced from the general equations in the previous section and are as follows:

Continuity Equation

$$\frac{1}{\rho}\frac{\partial \rho}{\partial t} + \frac{u}{\rho}\frac{\partial \rho}{\partial x} + \frac{\partial u}{\partial x} = 0$$

A.1

Equation of Motion

$$\rho\frac{\partial u}{\partial t} + \rho u\frac{\partial u}{\partial x} + \frac{\partial p}{\partial x} = 0$$

A.2

Energy Equation

$$\frac{\partial S}{\partial t} + u\frac{\partial S}{\partial x} = 0$$

A.3

Equation of State

$$p = p(\rho, S)$$

A.4

The equations (A.1 - A.4) form a system of quasilinear partial-differential equations of the hyperbolic type. An exact solution is in general not possible, but it is possible to reduce the equations to a total differential form by considering the variation of the unknown variables along certain directions known as the characteristic directions.

Introducing the speed of sound, c , as

$$c^2 = \left(\partial p / \partial \rho\right)_s \qquad \text{A.5}$$

we can write for the differential dp

$$dp = \left(\frac{\partial p}{\partial \rho}\right)_s d\rho + \left(\frac{\partial p}{\partial s}\right)_\rho ds = c^2 d\rho + \left(\frac{\partial p}{\partial s}\right)_\rho ds$$

Using this to eliminate derivatives of ρ in equation (A.1) we have:

$$\frac{\partial p}{\partial t} + u\frac{\partial p}{\partial x} + \rho c^2 \frac{\partial u}{\partial x} = 0 \qquad \text{A.6}$$

Adding and subtracting equation (A.6) from equation (A.2) gives:

$$\frac{\partial p}{\partial t} + \left(u+c\right)\frac{\partial p}{\partial x} + \rho c \left\{\frac{\partial u}{\partial t} + \left(u+c\right)\frac{\partial u}{\partial x}\right\} = 0$$

$$\frac{\partial p}{\partial t} + \left(u-c\right)\frac{\partial p}{\partial x} - \rho c \left\{\frac{\partial u}{\partial t} + \left(u-c\right)\frac{\partial u}{\partial x}\right\} = 0$$

$$\text{A.7}$$

and $\dfrac{\partial s}{\partial t} + u\dfrac{\partial s}{\partial x} = 0$

These equations become total differential equations along the following characteristic directions respectively:

$$
\begin{aligned}
(\lambda_1) \quad & \frac{dx}{dt} = u + c \\
(\lambda_2) \quad & \frac{dx}{dt} = u - c \\
(\lambda_3) \quad & \frac{dx}{dt} = u
\end{aligned}
\Bigg\}
\qquad \text{A.8}
$$

Along these characteristics the rate of change of the unknown variables p, u and S is given by:

$$
\begin{aligned}
\text{along} \ (\lambda_1) \quad & \frac{dp}{dt} + \rho c \frac{du}{dt} = 0 \\
\text{along} \ (\lambda_2) \quad & \frac{dp}{dt} - \rho c \frac{du}{dt} = 0 \\
\text{along} \ (\lambda_3) \quad & \frac{dS}{dt} = 0
\end{aligned}
\qquad \text{A.9}
$$

Note that the first two families of characteristic (λ_1 and λ_2) travel at the velocity of sound with respect to the fluid either with the flow (λ_1), or against it (λ_2). These are known respectively as right running or left running Mach lines.

The third family of characteristics (λ_3) is stationary with respect to the fluid. It is sometimes known as the regularity condition and imposes the constancy of entropy along a path-line. In cases of isentropic flow, the regularity condition is automatically satisfied since entropy is constant throughout the flow

not only on a path line. In all the further analysis

in this paper we will limit ourselves to isentropic

flow.

APPENDIX B

SIMPLE WAVES

Assuming isentropic flow, the first two equations of A.9 can be integrated in the form:

$$u + L(p) = 2r(\lambda_1)$$
$$u - L(p) = -2s(\lambda_2)$$

B.1

where $r(\lambda_1)$ and $s(\lambda_2)$ are arbitrary functions of the two characteristic directions λ_1 and λ_2 respectively. They are known as the Rieman invariants. The quantity L (p) is given by:

$$L(p) = \int_{p'}^{p} \frac{dp}{\rho c} = \int_{\rho'}^{\rho} \frac{c\,d\rho}{\rho}$$

B.2

where ρ' and p' are arbitrary constants.

A simple wave is now defined as a region where either r or s is constant. Taking as an example, the case $s(\lambda_2)$ = constant, then the λ_1 characteristics r = constant are straight. The wave thus propagates at velocity (u + c) and is right-running. In addition properties along the characteristic lines λ_1 are constant.

A fundamental property of simple waves is that a region adjacent to a state of constant properties will be a simple wave. For a more complete discussion of both simple waves and the method of characteristics see Ref. 9.

LIST OF REFERENCES

1) J.M. Walsh and R.H. Christian
    Equation of State of Metals from Shock Wave Measurements
    Physical Review, Vol. 97, No.6, March 1955

2) J.M. Walsh, M.H. Rice, R.G.McQueen and F.L. Yarger
    Shock-Wave Compressions of Twenty-Seven Metals. Equations
    of State of Metals.
    Physical Review, Vol. 108, No.2, October 1957

3) R.G. McQueen and S.P. Marsh
    Equation of State for Nineteen Metallic Elements from
    Shock-Wave Measurements to Two Megabars.
    J. Applied Physics, Vol. 31, No.7, July 1960

4) M.H. Rice, R.G. McQueen and J.M. Walsh
    Compression of Solids by Strong Shock Waves
    Solid State Physics, Vol. 6, Academic Press, 1958

5) L.V. Al'tshuler, S.B. Kormer, A.A. Bakanova and
    R.F. Trunin
    Equation of State for Aluminum, Copper and Lead in the
    High Pressure Region.
    Soviet Physics JETP, Vol. II, No.3, September 1960

6) L.V. Al'tshuler, A.A. Bakanova and R.F. Trunin
    Shock Adiabats and Zero Isotherms of Seven Metals at
    High Pressures.
    Soviet Physics JETP, Vol. 15, No.1, July 1962

7) L.V. Al'tshuler, S.B. Kormer, M.I. Brazhuik
    L.A. Vladimirov, M.P. Speranskaya and A.I. Funtikov
    The Isentropic Compressibility of Aluminum, Copper, Lead
    and Iron at High Pressures.
    Soviet Physics JETP, Vol. II, No.4, October 1960

8) B.J. Alder
    Physics Experiments with Strong Pressure Pulses from
    "Solids under Pressure" edited by W. Paul and D.M.
    Warschauer
    McGraw-Hill, 1963

9) R. Courant and K.O. Friedrichs
    Supersonic Flow and Shockwaves
    Interscience Publishers, 1948

10) J.C. Slater
    Introduction to Chemical Physics
    McGraw-Hill, 1939

11)   S.B. Kormer, V.D. Urlin and L.T. Popova
      Interpolation Equation of State and its Application
      to Experimental Data on Impact Compression of Metals.
      Sov. Phys. Solid State, Vol. 3, No.7, 1962.

12)   J.H. Tillotson
      Metallic Equation of State for Hypervelocity Impact
      General Atomic, GA-3216, 1962.

13)   G.V. Bull
      On the Impact of Pellets with Thin Plates
      McGill TN 1-10/61, 1961

14)   W.H. Friend, D.A. Miller and C.L. Murphy
      The Hypervelocity Impact of Pellets with Thin Plates:
      Theoretical Considerations, Part 2
      McGill Report 62-8, October 1962

15)   G.V. Bull, C.L. Murphy, F.J. Zwarts and W.H. Friend
      Review of Hypervelocity Impact Studies at McGill
      University
      McGill Report 63-15, December 1963

16)   C.J. Maiden
      Investigation of Fundamental Medanism of Damage to
      Thin Targets by Hypervelocity Projectiles.
      GM Defense Research Laboratories, TM 63-201, March 1963

17)   K.P. Stanyukovich
      Unsteady Motion of Continuous Media
      Pergamon Press, 1960

18)   P.C. Chou, H.S. Sidhu and L.J. Zajac
      Attenuation of the Strong Plane Shock Produced in a
      Solid by Hypervelocity Impact
      Drexel Institute of Technology Report 125-5, February 1964.

19)   F.L. Whipple
      The Meteoric Risk to Space Vehicles.
      Vistas in Astronautics, pp. 115-124, Pergamon Press, 1958.

20)   D.G. Doran, G.R. Fowles and G.A. Peterson
      Shock-Wave Compression of Aluminum
      Phys. Rev. Letters, Vol. I, No.11, p.402, December 1958

21)   J.M. Walsh and J.H. Tillotson
      Hydrodynamics of Hypervelocity Impact.
      General Atomic, Report GA-3827. Also in Proceedings of
      the Sixth Symposium on Hypervelocity Impact,
      Vol. II, Part 1, August 1963

22)   W.J. Rae and H.P. Kirchner
       Final Report on a Study of Meteoroid Impact Phenomena.
       Cornell Aeronautical Laboratory, Report RM-1655-M-4.
       February 1963.   Also in Proceedings of the Sixth
       Symposium on Hypervelocity Impact, Vol. II, Part 1,
       August 1963

23)   F.D. Murnaghan
       Finite Deformation of an Elastic Solid
       John Wiley and Sons, Inc. 1951

TABLE I

Polynomial Curve-Fit of Hugoniot Curve of Various Materials:

$$p = \sum_{n} a_n \left(\frac{\rho}{\rho_0} - 1 \right)^n \times 10^{10} \text{ dynes/cm}^2$$

a_n \ n	Aluminum	Copper	Lead	Iron
1	73.1	137.0	41.4	30.3
2	152.7	271.7	101.7	724.5
3	143.5	224.0	120.0	-271.2
4	-887	1078	-43	-14
5	2862	-2907	547	852
6	-3192	3674	-801	-----
7	1183	-1346	312	-----

TABLE II

Polynomial Curve-Fit of Isentropic Compressibility Behind
Shock:

$$K = \sum b_n \left(\frac{\rho}{\rho_0} - 1 \right)^{n-1} \times 10^{10} \text{ dynes/cm}^2$$

b_n \ n	Aluminum	Copper	Lead	Iron
1	73.1	137.0	41.4	196.3
2	305.4	543.4	203.4	-157.0
3	194.8	266.8	184.2	3862.2
4	-444	4037	248	-5448
5	519	-11745	-439	3077
6	-106	9650	167	-----

TABLE III

Equation-of-State Constants (Ref. 12)

Material	a	b	P_0	E_0	A	B	E_s	α	β
CH_2	0.6	2.0	0.92	7.0	7.5	2.0	2.4	10	5
Pb	0.4	2.37	11.34	1.5	46.64	15.0	0.26	13	15
W	0.5	1.04	19.17	22.5	308.0	250.0	1.4	10	10
Cu	0.5	1.5	8.90	32.5	139.0	110.0	2.0	5	5
Fe	0.5	1.5	7.86	9.5	127.9	105.0	2.5	5	5
Al	0.5	1.63	2.70	5.0	75.2	65.0	3.0	5	5
Be	0.55	0.62	1.85	17.5	117.34	55.0	10.0	5	5
Ti	0.5	0.60	4.50	7.0	103.0	50.0	3.5	5	5
Ni	0.5	1.33	8.86	9.0	191.2	150.0	3.0	5	5
Mo	0.5	1.02	10.20	4.5	271.3	165.0	3.0	5	5
Th	0.4	0.86	11.68	2.5	53.1	50.0	2.0	9	0.88